

***Revised Manuscript with no Changes Highlighted**

[Click here to download Revised Manuscript with no Changes Highlighted: beast_2019 -clean.pdf](#)

1 **Detect change-point, trend, and seasonality in satellite time series data to track abrupt changes**
2 **and nonlinear dynamics: A Bayesian ensemble algorithm**

3 Kaiguang Zhao^{1,2*}, Michael A. Wulder³, Tongxi Hu², Ryan Bright⁴, Qiusheng Wu⁵, Haiming Qin⁶,

4 Yang Li², Elizabeth Toman², Bani Mallick⁶, Xuesong Zhang⁷, and Molly Brown⁸

5 1. Ohio Agricultural Research and Development Center, School of Environment and Natural

6 Resources, The Ohio State University, Wooster, OH 44691, USA

7 2. School of Environment and Natural Resources, Environmental Science Graduate Program, The

8 Ohio State University, Columbus, OH 43210, USA

9 3. Canadian Forest Service, Natural Resources Canada, Victoria, British Columbia V8Z 1M5, Canada

10 4. Norwegian Institute of Bioeconomy Research (NIBIO), 1431 Ås, Norway

11 5. Department of Geography, Binghamton University, State University of New York, Binghamton,

12 NY 13902, USA

13 6. Department of Statistics, Texas A&M University, College Station, USA

14 7. Joint Global Change Research Institute, Pacific Northwest National Laboratory, University of

15 Maryland, College Park, MD, 20740, USA

16 8. Department of Geographical Sciences, University of Maryland, MD 20771, College Park, USA

17 * To whom all correspondence should be addressed (zhao.1423@osu.edu).

18 **Abstract:** Satellite time-series data are bolstering global change research, but their use to elucidate
19 land surface or vegetation dynamics is sensitive to algorithmic choices. Different algorithms often
20 give inconsistent or sometimes conflicting interpretations of the same data. This lack of consensus
21 has adverse implications and can be mitigated via ensemble modeling, an algorithmic paradigm that
22 combines many competing models rather than choosing only a single “best” model. Here we report
23 one such time-series decomposition algorithm for deriving nonlinear ecosystem dynamics across
24 multiple timescales—A Bayesian Estimator of Abrupt change, Seasonal change, and Trend
25 (BEAST). As an ensemble algorithm, BEAST quantifies the relative usefulness of individual
26 decomposition models, leveraging all the models via Bayesian model averaging. We tested it upon
27 simulated, Landsat, and MODIS data. BEAST reliably detected changepoints, seasonality, and trends
28 in the data; it derived realistic nonlinear trend signals and credible uncertainty measures (e.g.,
29 occurrence probability of changepoints over time)—some information difficult to derive by
30 conventional single-best-model algorithms but critical for interpretation of ecosystem dynamics and
31 detection of low-magnitude disturbances. The combination of many models enabled BEAST to
32 alleviate model misspecification, address algorithmic uncertainty, and reduce overfitting. BEAST is
33 generically applicable to time-series data of all kinds, serving to improve robustness in uncovering
34 true time-series dynamics. It offers a new analytical option for changepoint detection and nonlinear
35 trend analysis and will help exploit environmental time-series data for probing patterns and drivers of
36 ecosystem dynamics.

37 **Keywords:** *Changepoint; Bayesian changepoint detection; Disturbance ecology; Breakpoint; Trend*
38 *analysis; Time series decomposition; Bayesian model averaging; Disturbances; Nonlinear dynamics; Regime*
39 *shift*

40 1. Introduction

41 Ecosystems are changing constantly, driven by natural forcings and human activities in
42 complex ways. Disentangling the complexity to build predictive biospheric sciences is a defining
43 theme of global change research (*Franklin et al. 2016*)—a goal hard to attain without reliable
44 capabilities of monitoring lands over time (*Pettorelli et al. 2014; Su et al. 2016; Zhao and Jackson 2014*).
45 To date, such spatiotemporal data come primarily from satellites (*Hu et al. 2017; Jetz et al. 2016*).
46 Satellite time-series data, such as decades of Landsat, MODIS, or AVHRR imagery, have proven
47 particularly valuable for elucidating patterns and drivers of land and ecosystem dynamics (*Hawbaker*
48 *et al. 2017; Li et al. 2018; Zhu and Woodcock 2014*).

49 Despite existing successes in satellite time-series analyses, challenges remain. A notable issue
50 pertains to the diverging findings from the use of satellite data in addressing the same problem. For
51 example, there is controversy regarding how the Amazon forests respond to basin-wide droughts;
52 some satellite analyses suggested a green-up but others not (*Huete et al. 2006; Samanta et al. 2010*).
53 Inconsistencies like this are attributed partly to different algorithms and perspectives taken for data
54 processing and analysis (*Liu et al. 2018; Shen 2011; Tewkesbury et al. 2015*). A preponderance of
55 satellite time-series analyses take a statistical modeling perspective, seeking a so-called best model out
56 of many candidates to decompose time series into vegetation dynamics such as trends and abrupt
57 changes (*Cai et al. 2017; Jonsson and Eklundh 2002*). This single-best-model paradigm is broadly
58 embraced by practitioners (*Powell et al. 2010; Zhao et al. 2018*), but its use for seeking mechanistic
59 understandings of ecosystems is not necessarily safe (*Chen et al. 2014; Grossman et al. 1996*).

60 Mechanistic interpretations of time-series data are sensitive to choices of statistical
61 algorithms or models. When fitting a linear model to decades of AVHRR data, a greening trend in
62 vegetation was inferred and was attributed to global warming (*Myneni et al. 1997*). If using a piecewise
63 linear model with one changepoint instead, a greening was observed only for the first period whereas

64 a browning for the second, generating new explanations of climate-biosphere interactions (*Wang et al.*
65 *2011*). If piecewise models with multiple changepoints were fitted, the conclusion would change
66 again, giving alternative speculations on drivers of ecosystem changes (*Jong et al. 2012*). Similar
67 studies with diverging findings abound (*Alcaraz-Segura et al. 2010; Yu et al. 2010*). Extrapolation from
68 such findings is at stake if applied blindly to validate predictive models and inform resource
69 management.

70 Inconsistent or contradicting insights gained from different models are a common problem of
71 the single-best-model paradigm. The “best” models are often selected to optimize certain criteria
72 such as AIC and BIC. Depending on data quality and the choices of optimization algorithms and
73 model selection criteria, many “best” models are possible for the same time series (*Banner and Higgs*
74 *2017; Cade 2015*). The usefulness of these models is not dichotomous. Favoring one against others is
75 an over-simplifying strategy that often overlooks the utility of alternative models and ignores model
76 uncertainties. Model selection in the single-best-model paradigm is also complicated by the
77 subjectivity in specifying data analysis models and the inability of simple models to represent complex
78 time-series signals. Model structures with increased complexity are more likely to capture variations
79 in satellite data at multiple timescales, but they are also more likely to overfit the data and their
80 estimation entails sophisticated statistical techniques.

81 Many problems difficult to tackle by conventional methods can now be addressed by turning
82 to Bayesian statistics—an inferential paradigm that can treat both model parameters and structures
83 probabilistically and offer a unified framework to address uncertainties of various forms (*Denison*
84 *2002; Ellison 2004; Finley et al. 2007; Zhao et al. 2008; Zhou et al. 2017*). Unlike conventional
85 criterion-based methods that choose only a single best model, the Bayesian paradigm can embrace all
86 candidate models, evaluate how probable each of them is a true one, and synthesize the many models
87 into an average model (*Denison 2002; Thomas et al. 2018; Zhao et al. 2013*). This scheme is known as

88 Bayesian model averaging (BMA). It belongs to a category of multi-model techniques broadly called
89 ensemble learning. Consideration of many models helps BMA to capture model uncertainty, alleviate
90 model misspecification, and improve flexibilities and generalizability in modeling complex data.
91 These advantages of BMA have been exemplified in numerous case studies across disciplines (*Banner*
92 *and Higgs 2017; Raftery et al. 2005; Zhang and Zhao 2012; Zhao et al. 2013*). Despite all the benefits of
93 Bayesian inference or BMA, its use for satellite time-series analysis remains rather limited, with
94 enormous potential to tap.

95 This study seeks to reliably decipher time-series data for via Bayesian modeling. Our aim is
96 (1) to introduce a generic Bayesian time-series decomposition algorithm for changepoint detection
97 and nonlinear trend analysis, and (2) to demonstrate its applications to satellite data for tracking land
98 and ecosystem nonlinear dynamics. We term the algorithm BEAST—a Bayesian Estimator of Abrupt
99 change, Seasonality, and Trend. BEAST features many advantages over conventional non-Bayesian
100 algorithms. Foremost, it forgoes the single-best-model paradigm and applies the Bayesian ensemble
101 modeling technique to combine numerous competing models and generate a rich set of information
102 unobtainable from non-Bayesian algorithms. BEAST can quantify various sources of uncertainties,
103 detect abrupt changes of any magnitude, and uncover complex nonlinear dynamics from time-series
104 data. But due to the Bayesian computation needed, its applications to high-resolution imagery over
105 large areas may be constrained by computer power.

106 In what follows, we further justify the value of Bayesian statistics for time-series analysis
107 (Sect 2; Fig. 1), then detail the formulation of our BEAST algorithm (Sect 3; Figs. 2-3), and test the
108 capabilities of BEAST using both simulated and real data (Sect 4 & 5; Figs. 4-11). We also discuss the
109 many features of BEAST as contrasted to existing time-series decomposition algorithms, and explain
110 how ensemble learning and Bayesian modeling help to make BEAST a useful tool to capture,
111 monitor, and derive land surface dynamics from satellite data (Sect 6).

112 2. Why use Bayesian statistics?

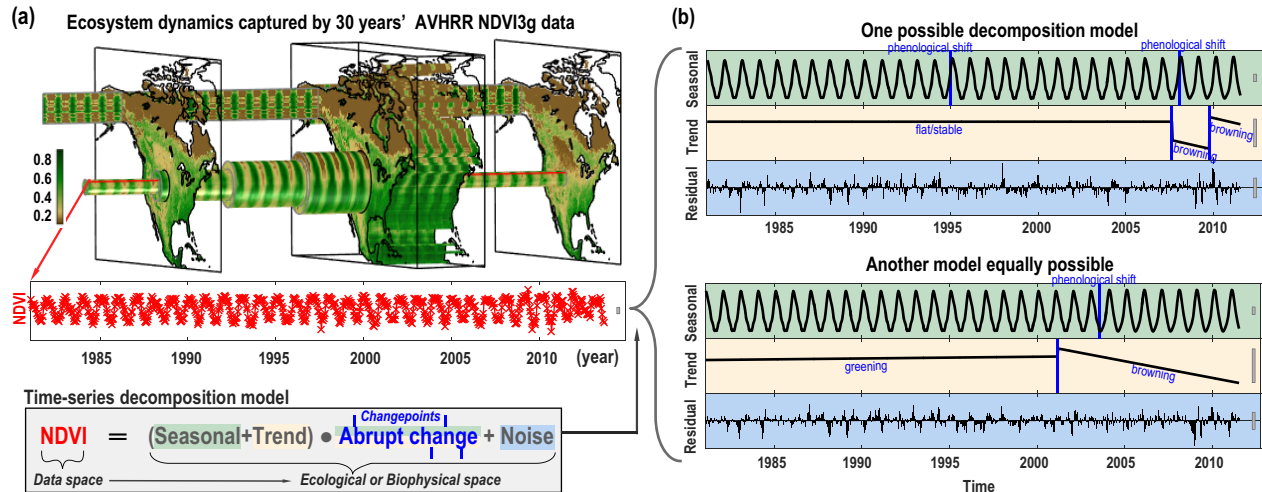
113 We begin with extra backgrounds on how time-series data have been conventionally decomposed in
114 non-Bayesian frameworks. Their potential weaknesses are then detailed to justify the needs for
115 Bayesian algorithms. Below, our presentation focuses on time series of Normalized Difference
116 Vegetation Index (NDVI)—a spectral variable measuring land surface greenness or vegetation vigor
117 (Fig. 1a). But the reasoning applies equally to non-NDVI or non-satellite data, such as LAI, albedo,
118 climate, streamflow, and social-ecological indicators.

119 Ecologically speaking, a NDVI time series captures landscape dynamics at three major
120 timescales (*Kennedy et al. 2014*): (1) seasonality or periodic variations as forced by intra-annual
121 climatic variations or phenological drivers; (2) gradual changes as driven by long-term environmental
122 trends, chronic disturbances, or successional dynamics; and (3) abrupt changes associated with severe
123 disturbances, sudden recoveries, regime shifts, or altered management practices (e.g., fire, insect,
124 logging, weeding, urbanization, re-vegetation, extreme weather, crop rotation, and climate shift). In
125 this decomposition, the time series is treated as the sum of the first two components—seasonal and
126 trend signals (Fig. 1b). The third component—abrupt changes—do not stand out alone but is
127 embedded in seasonality and trends as changepoints (Fig. 1b, blue vertical bars).

128 Mathematically speaking, the search for ecological interpretations of a time series reduces to
129 finding the relationship between NDVI (y) and time (t) from the observed data at n points of time
130 $\mathcal{D} = \{t_i, y_i\}_{i=1, \dots, n}$ via a statistical model $\hat{y}(t) = f(t)$. The model generally treats the time series
131 $y(t_i)$ as an addition of seasonal $S(\cdot)$ and trend $T(\cdot)$ signals (Fig. 1):

$$\hat{y}(t_i) = f(t_i; \Theta) = S(t_i; \Theta_s) + T(t_i; \Theta_T), \mathbf{i}=1, \dots, \mathbf{n} \quad (1)$$

132 where the parameters Θ_s and Θ_T specify the seasonal and trend signals; they also encode the abrupt
133 changes implicitly. By analogy to linear regression, the time t and data y are independent and
134 dependent variables, respectively; Θ_s and Θ_T are parameters to be estimated from the data \mathcal{D} .



135
 136 Fig. 1. Tracking land surface dynamics from space is treated here as a time-series decomposition problem. (a) A 3D
 137 volumetric view of 30 years of AVHRR NDVI data depicts ecosystem dynamics at three timescales: seasonality,
 138 trend (e.g., climate-driven responses or successional dynamics), and abrupt change (e.g., disturbance or
 139 changepoint). Algorithmically speaking, decomposition of a time series into these three components is a model
 140 selection problem, seeking an “optimal” model structure that best fits the time series. (b) But the use of different
 141 inferential procedures or selection criteria yields different or even contradictory decompositions, with adverse
 142 implications. For example, two “optimal” models in (b) can fit the same time series of (a) almost equally well, but
 143 with inconsistent decompositions and ecological interpretations. Vertical blue bars denote changepoints in seasonal
 144 dynamics or trends. The equal plausibility of the two “best” models highlights an inherent weakness of many
 145 existing satellite time-series analyses for studying ecosystem changes.

146 By decomposing a time series with Eq. 1, we seek to answer the following questions:

147 (1) How many changepoints occur and when? Changepoints indicates any abrupt changes in
 148 trend/seasonal signals (*Jamali et al. 2015*). By “abrupt”, we refer to not only sudden NDVI jumps
 149 (e.g., forest clearing or quick recovery) but also any turning points or breakpoints at which trend or
 150 seasonal signals start to deviate from the previous regular trajectories. This definition is broader and
 151 more inclusive than that assumed by other algorithms. As examples, a smooth recovery from tree
 152 stand-clearing is often associated with only one changepoint by many algorithms, but in our
 153 definition, the recovery trajectory may have many changepoints related to different succession stages

154 or rates of recovery. A subtle transition in vegetation dynamics caused by a shift in climate regime is
155 rarely considered as a changepoint by many algorithms, but in our definition it is.

156 (2) What is the underlying trend? A trend is not just a linear line but can be a complex
157 nonlinear trajectory interspersed with changepoints. The transient trend trajectory at changepoints
158 are rarely true discontinuous jumps but rather quasi-continuous sharp transitions. Detection of trends
159 with high fidelity is critical for inferring subtle drivers of ecosystem dynamics (e.g., climatic effects).

160 (3) What is the underlying seasonal signal? A seasonal signal may be also interspersed by
161 changepoints. Seasonal changepoints do not necessarily coincide with trend changepoints. Detection
162 of seasonal changepoints helps to identify potential drivers of phenology changes.

163 Any uncertainties or errors in inferring the model Eq. 1 will be translated to those in answering these
164 questions, thereby engendering contradictory or wrong ecological insights into ecosystem dynamics.

165 Existing methods to infer the model or relationship f come in many fashions (*Brooks et al.*
166 *2014; Kennedy et al. 2010; Zhu and Woodcock 2014*). Often, the trend is parameterized and
167 approximated by linear, piecewise-linear, or polynomial models (*Browning et al. 2017*). The seasonal
168 signal is modeled via flexible basis functions, such as Fourier curves and wavelets (*Brooks et al. 2012;*
169 *Jiang et al. 2010; Martínez and Gilabert 2009; Shu et al. 2017*). Another alternative is to ignore
170 seasonal signals by fitting a trend model to a sub-time series (e.g., summertime NDVI only) (*Wang et*
171 *al. 2011*). Moreover, abrupt NDVI changes are implicitly encoded in the parameters Θ_T and Θ_S .
172 These changepoints also need to be inferred from the data \mathcal{D} (*Chen et al. 2014*). Such diverse options
173 for model configurations lead to a large or even infinite number of candidate models for analyzing the
174 same time series. Conventional methods aim to seek the “best” model and discard others based on
175 selection criteria, such as mean square error, Cp, AIC, anomaly threshold, or subjective criteria (*Chen*
176 *et al. 2014; Wang et al. 2011*).

177 These conventional methods have potential weaknesses that were not always articulated in
178 previous studies (Fig. 1). First, vegetation dynamics normally shows a nonlinear trend (*Burkett et al.*
179 *2005; Jentsch et al. 2007*), which is not guaranteed to be adequately approximated by a single linear,
180 piecewise-linear, or polynomial model. Second, many conventional analyses make too restrictive
181 model assumptions. For example, prior studies often assumed a prescribed number of changepoints
182 or a fixed harmonic order in seasonality (*Lu et al. 2004; Wang et al. 2011*), which is too arbitrary a
183 choice. Third, the true model for NDVI dynamics is essentially unknown so that model
184 misspecification is inevitable (*Kennedy and O'Hagan 2001*). The use of misspecified or wrong models
185 is of little concern for those applications on retrievals of biophysical variables (*Shmueli 2010; Zhao et*
186 *al. 2018*), but it becomes problematic for ecological interpretation of NDVI data simply because
187 different models imply contrasting or contradicting hypotheses. Such model uncertainties are
188 typically ignored by non-Bayesian approaches.

189 Fourth, even for the same class of model type, the final model chosen is sensitive to not only
190 model selection criteria but also data noises, thus opening up possibilities for inconsistent
191 interpretations. The hyper-sensitivity of model inference to data noises has been widely recognized
192 and reported in the literature of various disciplines (*Grossman et al. 1996; Oreskes et al. 1994; Zhao et*
193 *al. 2013*). Fifth, the number of all possible models is often enormous, making it computationally
194 infeasible to evaluate all of them. Instead, efficient approaches, such as forward sweep, greedy
195 searching, and genetic algorithms, come into play to evaluate a finite selection of models with regards
196 to some optimization schemes, but these schemes tend to find sub-optimal solutions (*Denison 2002*).
197 Sixth, diagnostic statistics generated using conventional approaches are inadequate for answering
198 many practical questions (e.g., what is the probability of seeing an abrupt change in the year 2002?).

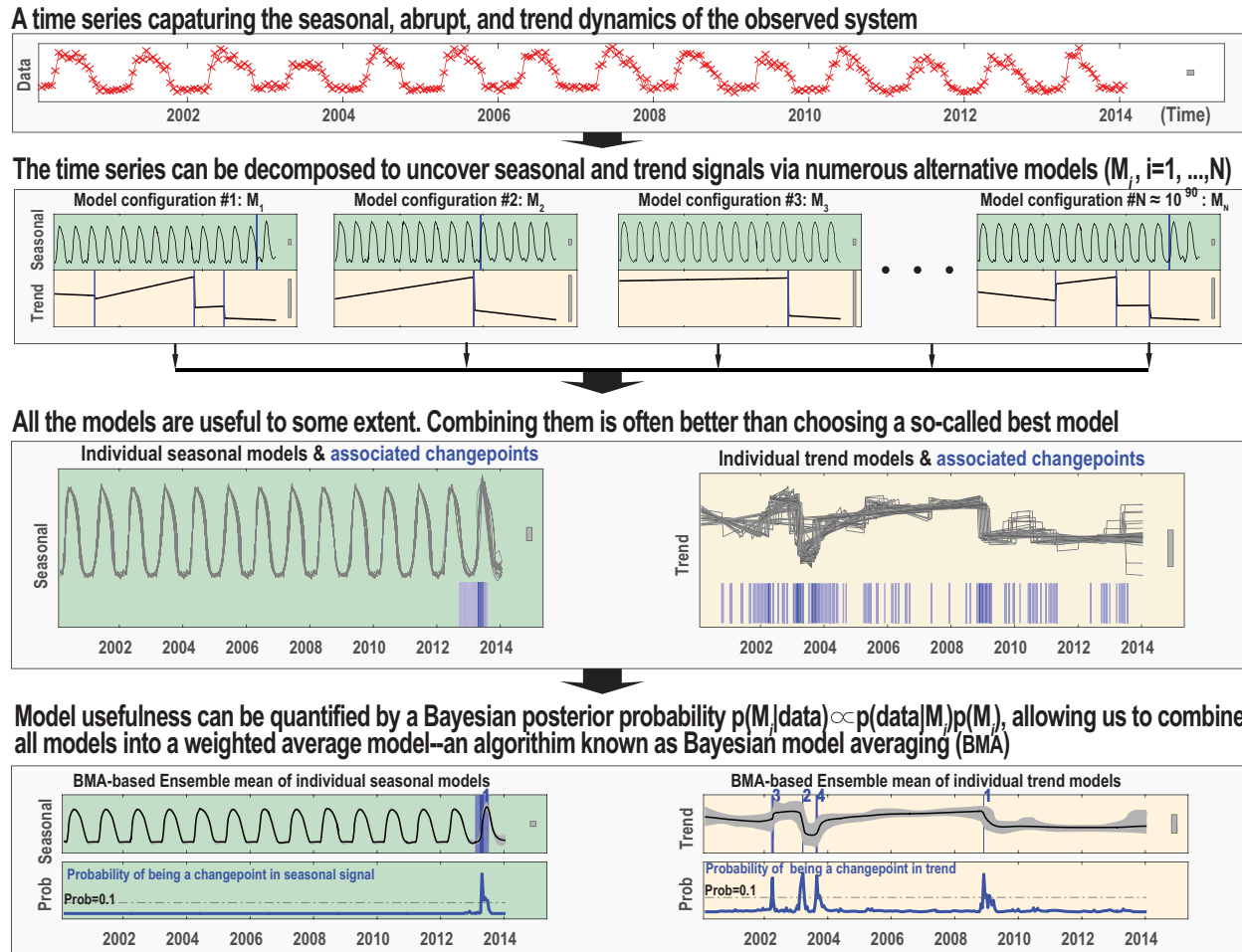
199 These potential limitations of conventional statistical modeling can be alleviated by switching
200 from the conventional single-best-model paradigm to the Bayesian paradigm (Fig. 2). Advantages of

201 the Bayesian paradigm are being demonstrated by a growing body of theoretical and empirical
202 evidence (*Denison 2002; Rankin et al. 2017; Reiche et al. 2015; Zhao et al. 2013; Zhou et al. 2017*).
203 Foremost, Bayesian inference treats both model parameters and structures as random and therefore
204 characterizes them explicitly and probabilistically. As such, Bayesian inference tends not to deem any
205 single model configuration as the true model, but instead recognizes the relevance and usefulness of
206 all the potential models (*Kennedy and O'Hagan 2001; Zhao et al. 2013*). Specifically, each model is
207 assigned a probability being the true model (Fig. 2); this probability can be learned from data and then
208 used as an informative weight to synthesize all the models into a weighted average model. This
209 Bayesian model averaging scheme is flexible enough to approximate complex relationships that
210 cannot be represented by individual models (Fig. 2). It also alleviates the adverse consequences of
211 model misspecification and tackles model uncertainty (*Zhao et al. 2013*).

212 Computationally, Bayesian inference or BMA is implemented via stochastic sampling
213 algorithms known as Markov Chain Monte Carlo (MCMC) (*Denison 2002; Green 1995*). MCMC
214 sampling helps to effectively explore the enormous model space at a reasonable computation cost.
215 The use of MCMC circumvents analytical intractability and enables the Bayesian paradigm to handle
216 the complexity that conventional methods cannot handle. MCMC also generates various sample-
217 based statistics to test hypotheses that are difficult to tackle using the conventional paradigm.

218 Bayesian statistics can aid in inferring the model of Eq. 1, due especially to its additive nature:
219 a time series is the sum of seasonal and trend signals, with changepoints being inseparable parts of
220 them. Inference of the three— trend, seasonality, and changepoints,—is not separable. Any
221 estimation error in one will be leaked to bias the estimation of others. It is unlikely to correctly detect
222 changepoints if the trend or seasonality is not well modelled. Trend analysis and changepoint
223 detection are two sides of the same goal. It is also impossible to estimate true decomposition
224 uncertainties if not accounting for model misspecification simultaneously for the three components.

225 Therefore, reliable time-series decomposition requires sufficiently approximating the nonlinearity of
 226 both trend and seasonality and simultaneously incorporating model uncertainties of all sorts. These
 227 issues are explicitly tackled by Bayesian inference, as detailed next.



228
 229 Fig. 2. Illustration of BEAST—a Bayesian ensemble time-series decomposition algorithm. Our modeling philosophy
 230 is that a time series can be fitted by numerous competing models, all of which are wrong but useful to some degree.
 231 Conventional methods choose the “best” model, ignoring model uncertainty or misspecification and opening up
 232 room for fortuitous conclusions (Fig. 1). As a remedy, BEAST quantifies the relative usefulness of individual models
 233 (i.e., model structures) and incorporates all the models into the inference via Bayesian model averaging. This
 234 ensemble learning makes BEAST a universal approximator of complex nonlinear trends and allows BEAST to
 235 account for uncertainties difficult to consider by non-Bayesian methods. For example, model uncertainty is explicitly
 236 addressed (e.g., gray envelope around the fitted seasonal or trend signals are 95% credible intervals). BEAST not only

237 detects the changepoints but also quantifies their probabilities of being true changepoints, providing confidence
 238 measures to guide informative interpretation of satellite time-series data.

239 3. BEAST: Bayesian estimator of abrupt change, seasonality & trend

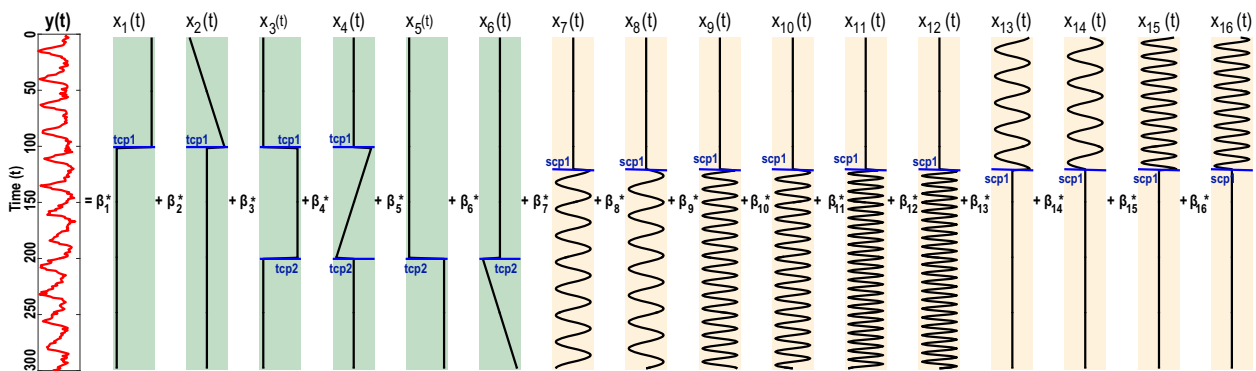
240 This section describes the formulation and implementation of our BEAST time-series decomposition
 241 algorithm. The description is inevitably mathematical. Readers not interested in technical specifics
 242 may skip to Section 4 while re-visiting Figs. 2 & 3 or Section 2 for an overview of the concept and
 243 capabilities of BEAST. The implemented software is available as both a Matlab library and an R
 244 package (*to be released upon acceptance of this ms*).

245 3.1 Parametric form of BEAST for time-series decomposition

246 Our analysis considers a time series $\mathcal{D} = \{t_i, y_i\}_{i=1, \dots, n}$ to be composed of three
 247 components—seasonality, trend, abrupt changes—plus noise (Fig. 1b), which is formulated as a
 248 rewriting of Eq. 1:

$$y_i = S(t_i; \Theta_s) + T(t_i; \Theta_T) + \varepsilon_i. \quad (2)$$

249 Here, we assume the noise ε to be Gaussian, capturing the remainder in the data not explained by the
 250 seasonal $S(\cdot)$ and trend $T(\cdot)$ signals. Following the common practice, we adopted general linear
 251 models to parameterize $S(\cdot)$ and $T(\cdot)$ (*Jiang et al. 2010; Verbesselt et al. 2010b*). Abrupt changes are
 252 implicitly encoded in the parameters Θ_s and Θ_T of the seasonal and trend signals.



BEAST adopts a general linear model for time-series decomposition:

$$y = \beta_1^* x_1 + \beta_2^* x_2 + \beta_3^* x_3 + \beta_4^* x_4 + \beta_5^* x_5 + \beta_6^* x_6 + \beta_7^* x_7 + \beta_8^* x_8 + \beta_9^* x_9 + \beta_{10}^* x_{10} + \beta_{11}^* x_{11} + \beta_{12}^* x_{12} + \beta_{13}^* x_{13} + \beta_{14}^* x_{14} + \beta_{15}^* x_{15} + \beta_{16}^* x_{16}$$

Matrix Form $\rightarrow y = X_M \beta_M$ where model structure $M =$ { number and timings of trend changepoints (tcp), number and timings of seasonal changepoints (scp), harmonic orders of individual seasonal segments }

1st trend segment

2nd trend segment

3rd trend segment

1st seasonal segment
(3rd-order harmonic: 6 terms)

2nd seasonal segment
(2nd-order harmonic: 4 terms)

253

254 Fig. 3. How does BEAST decompose time series? BEAST is an additive model $y = X_M \beta_M$, formulating a time
 255 series $y(t)$ as the linear combination of many basis functions X_M (e.g., line segments x_1-x_6 or harmonics x_7-x_{16} that are
 256 zero-valued except for the active segments). These basis terms are specified by the model structure parameters M :
 257 numbers and locations of seasonal/trend changepoints (i.e., horizontal blue bars such as $tcp1$ and $scp1$) and seasonal
 258 harmonic orders (e.g., 3rd and 2nd in this example). The aim is to infer not only the coefficients β_M for a given M
 259 but also the model structure M itself (i.e., changepoint and harmonic orders). The combinatorics of all possible
 260 changepoints and harmonic orders gives an enormous model space with numerous candidate basis terms, making it
 261 computationally impossible to pinpoint the true best model. BEAST infers M by randomly traversing the model
 262 space via Bayesian model selection, so it is essentially a Bayesian general linear regression model. (The time axis is
 263 oriented vertically for ease of displaying.)

264 Specifically, the seasonal signal $S(t)$ is approximated as a piecewise harmonic model, defined
 265 with respect to p knots in time at $\xi_k, k=1, \dots, p$ (Fig. 3). These knots divide the time series into $(p+1)$
 266 intervals $[\xi_k, \xi_{k+1}], j=0, \dots, p$, where $\xi_0 = t_0$ and $\xi_{p+1} = t_n$ are the starting and ending times of the
 267 data. The model is specified for each of the $(p+1)$ segments $[\xi_k, \xi_{k+1}], k=0, \dots, p$, taking the form of

$$268 \quad S(t) = \sum_{l=1}^{L_k} a_{k,l} \sin\left(\frac{2\pi lt}{P}\right) + b_{k,l} \cos\left(\frac{2\pi lt}{P}\right) \text{ for } \xi_k \leq t < \xi_{k+1}, k = 0, \dots, p$$

269 Here, P is the period of the seasonal signal (i.e., one year in our cases); L_k is the harmonic order for
 270 the k -th segment and is an unknown segment-specific parameter; and the coefficients
 271 $\{a_{k,l}, b_{k,l}\}_{l=1, \dots, L_k}$ are the parameters for sines and cosines. This harmonic model is non-continuous as a
 272 whole; the knots ξ_k indicate the changepoints at which abrupt seasonal changes may occur. Both the
 273 total number of changepoints p and their timings $\{\xi_k\}_{k=1, \dots, p}$ are unknown parameters to be
 274 estimated. In short, we need the following parameters to fully specify the seasonal harmonic curve:

$$275 \quad \Theta_s = \{p\} \cup \{\xi_k\}_{k=1, \dots, p} \cup \{L_k\}_{k=0, \dots, p} \cup \{a_{k,l}, b_{k,l}\}_{k=0, \dots, p; l=1, \dots, L_k}$$

276 which includes the number and timings of changepoints, the harmonic orders for all the $(p+1)$
 277 segments, and the coefficients of all the harmonic terms. All have to be estimated.

278 The trend $T(t)$ is modeled as a piecewise linear function with respect to m knots at τ_j ,
 279 $j=1, \dots, m$ (Fig. 3), which divide the time span into $(m+1)$ intervals $[\tau_j, \tau_{j+1}]$, $j=0, \dots, p$, with $\tau_0 = t_0$ and
 280 $\tau_{m+1} = t_n$ being the start and end of the time series. The trend knots or changepoints τ_j are not
 281 necessarily the same as the seasonal changepoints ξ_k . The trend over each interval simply is a line
 282 segment (Fig. 2), defined by coefficients a_j and b_j :

$$283 \quad T(t) = a_j + b_j t \quad \text{for } \tau_j \leq t < \tau_{j+1}, j = 0, \dots, m$$

284 Similar to the seasonal signal, the number of changepoints m and their timings $\{\tau_j\}_{j=1, \dots, m}$ are
 285 unknown parameters to estimate. Hence, the full set of parameters specifying the trend T is

$$286 \quad \Theta_T = \{m\} \cup \{\tau_j\}_{j=1, \dots, m} \cup \{a, b_j\}_{j=0, \dots, m}$$

287 which comprises the number and timings of trend changepoints and the intercepts and slopes of
 288 individual line segments.

289 Both sets of the parameters, Θ_s and Θ_T , need to be estimated from the data \mathcal{D} . For ease of
 290 presentation, we re-classified the parameters Θ_T and Θ_s into two groups (Fig. 3): $\{\Theta_T, \Theta_s\} = \{M, \beta_M\}$.
 291 The first group M refers to model structure, including numbers and timings of trend and seasonal
 292 changepoints, and seasonal harmonic orders:

$$293 \quad M = \{m\} \cup \{\tau_j\}_{j=1, \dots, m} \cup \{p\} \cup \{\xi_k\}_{k=1, \dots, p} \cup \{L_k\}_{k=0, \dots, p}.$$

294 The second group β_M is the segment-specific coefficient parameters used to determine exact shapes
 295 of the trend and seasonal curves once the model structure M is given. Collectively, β_M is denoted by

$$296 \quad \beta_M = \{a, b_j\}_{j=0, \dots, m} \cup \{a_{k,l}, b_{k,l}\}_{k=0, \dots, p; l=1, \dots, L_k}.$$

297 The subscript M indicates the dependence of β_M on model structure M .

298 After this re-grouping, the original general linear model Eq. 2 becomes a familiar form:

$$y(t_i) = \mathbf{x}_M(t_i) \beta_M + \varepsilon_i \quad (3)$$

299 where $\mathbf{x}_M(t_i)$ and $\boldsymbol{\beta}_M$ are dependent variables and associated coefficients, respectively. Again, the
 300 subscript M suggests that the exact form of \mathbf{x}_M and the coefficients in $\boldsymbol{\beta}_M$ both depend on the model
 301 structure M (e.g., numbers and timings of changepoints). For example, column vectors of the design
 302 matrix $\mathbf{x}_M(t_i)$ are associated with individual segments of the piecewise linear and harmonic models
 303 (Fig. 3), with the number of coefficients in $\boldsymbol{\beta}_M$ being $2(m + 1) + 2 \sum_{k=0}^p L_k$.

304 As revealed in the re-formulated model of Eq. 3, the inference of vegetation dynamics now
 305 reduces to a model selection problem—determining an appropriate model structure M, including the
 306 numbers and timings of changepoints and the harmonic orders. Identifying an optimal model
 307 structure M for our problem is analogous to choosing the best subset of variables for simple linear
 308 regression. Once a model structure M is selected, its coefficients $\boldsymbol{\beta}_M$ are straightforward to estimate.
 309 However, unlike simple linear regression, the number of possible model structures for Eq. 3 is
 310 extremely large. Even for a time series of moderate length (e.g., $n > 100$), it takes billions of years'
 311 computation to enumerate all possible models for finding the best one that optimizes certain criteria
 312 (e.g., BIC). We circumvented this problem by resorting to Bayesian inference, as described next.

313 **3.2 Bayesian formulation of BEAST**

314 We extended the general linear model of Eq. 2 or 3 to build a Bayesian model for detecting
 315 abrupt change, seasonality, and trend from time-series data. In the Bayesian modeling, all the
 316 unknown parameters are considered random, including model structure M, coefficients $\boldsymbol{\beta}_M$, and data
 317 noise σ^2 . Given a time series $\mathcal{D} = \{t_i, y_i\}_{i=1, \dots, n}$, the goal is to get not just the best possible values of
 318 these parameters but more importantly, their posterior probability distribution $p(\boldsymbol{\beta}_M, \sigma^2, M | \mathcal{D})$. By
 319 Bayes' theorem, this posterior is the product of a likelihood and a prior model:

$$p(\boldsymbol{\beta}_M, \sigma^2, M | \mathcal{D}) \propto p(\mathcal{D} | \boldsymbol{\beta}_M, \sigma^2, M) \pi(\boldsymbol{\beta}_M, \sigma^2, M). \quad (4)$$

320 Here, the likelihood $p(\mathcal{D} | \boldsymbol{\beta}_M, \sigma^2, M)$ is the probability of observing the data \mathcal{D} given the model
 321 parameters $\boldsymbol{\beta}_M, \sigma^2$, and M. Its form is governed by the general linear model $y = \mathbf{x}_M \boldsymbol{\beta}_M + \varepsilon$ in Eq. 3.

322 Owing to the normality of error ε , the likelihood is simply Gaussian $p(\mathcal{D}|\boldsymbol{\beta}_M, \sigma^2, M) =$
 323 $\prod_{i=1}^n N(y_i; \mathbf{x}_M(t_i)\boldsymbol{\beta}_M, \sigma^2)$.

324 To complete our Bayesian formulation, what remains is to specify the second term of Eq. 4,
 325 $\pi(\boldsymbol{\beta}_M, \sigma^2, M)$, which is called the prior distribution of the model parameters. By definition, we have
 326
$$\pi(\boldsymbol{\beta}_M, \sigma^2, M) = \pi(\boldsymbol{\beta}_M, \sigma^2|M)\pi(M)$$
.

327 Therefore, it suffices to elicit the conditional prior $\pi(\boldsymbol{\beta}_M, \sigma^2|M)$ and the model prior $\pi(M)$
 328 separately. The priors encode our existing knowledge or beliefs in possible values of the model
 329 parameters. Because of a lack of such general knowledge beforehand, our choices are flat priors, close
 330 to being non-informative. First, for $\pi(\boldsymbol{\beta}_M, \sigma^2|M)$, we considered the normal-inverse Gamma
 331 distribution and introduced an extra dispersion hyperparameter ν into it to further reflect our vague
 332 knowledge of the magnitude of model coefficients $\boldsymbol{\beta}_M$. Second, for the prior on model structure
 333 $\pi(M)$, we assumed that the numbers of changepoints are any nonnegative integers that are equally
 334 probable a priori. The exact formula of our priors are detailed in Appendix A.

335 Given our likelihood and prior models, the posterior of the model parameters becomes
 336
$$p(\boldsymbol{\beta}_M, \sigma^2, \nu, \mathbf{M}|\mathcal{D}) \propto \prod_{i=1}^n N(y_i; \mathbf{x}_M(t_i)\boldsymbol{\beta}_M, \sigma^2) \pi_\beta(\boldsymbol{\beta}_M, \sigma^2, \nu|\mathbf{M})\pi(\mathbf{M}). \quad (5)$$

337 Its complete formulation after incorporating each component prior is expanded and presented in
 338 Appendix A, with more technical details explained there for interested readers.

338 **3.3 Monte Carlo-based Inference**

339 The posterior distribution $p(\boldsymbol{\beta}_M, \sigma^2, \nu, \mathbf{M}|\mathcal{D})$ of Eq. 5 encodes all the information essential for
 340 inferring ecosystem dynamics. But it is analytically intractable, so we resorted to MCMC sampling to
 341 generate a realization of random samples for posterior inference. The MCMC sampling algorithm we
 342 used is a hybrid sampler that embeds a reverse-jump MCMC sampler (RJ-MCMC) into a Gibbs
 343 sampling framework, as briefly described below.

344 The Gibbs framework samples the following three conditional posterior distributions in
 345 alteration for a total of N iterations.

$$\begin{aligned}
 & p(\mathbf{M}^{(i+1)} | \nu^{(i)}, \mathcal{D}); \\
 & p(\boldsymbol{\beta}_{\mathbf{M}}^{(i+1)}, \sigma^{2(i+1)} | \nu^{(i)}, \mathbf{M}^{(i+1)}, \mathcal{D}); \\
 & p(\nu^{(i+1)} | \boldsymbol{\beta}_{\mathbf{M}}^{(i+1)}, \sigma^{2(i+1)}, \mathbf{M}^{(i+1)}, \mathcal{D});
 \end{aligned} \tag{6}$$

346 These three conditional posteriors permit generating the (i+1)-th sample
 347 $\{\mathbf{M}^{(i+1)}, \boldsymbol{\beta}_{\mathbf{M}}^{(i+1)}, \sigma^{2(i+1)}, \nu^{(i+1)}\}$ from the previous sample $\{\mathbf{M}^{(i)}, \boldsymbol{\beta}_{\mathbf{M}}^{(i)}, \sigma^{2(i)}, \nu^{(i)}\}$. In particular, the
 348 second and third conditional posteriors are a normal-inverse Gamma distribution and a Gamma
 349 distribution (Appendix A), which are easy to sample. In contrast, the first conditional posterior
 350 $p(\mathbf{M}^{(i+1)} | \nu^{(i)}, \mathcal{D})$ is difficult to sample because it is defined only up to an unknown proportionality
 351 constant (Appendix A) and also because the dimension of M varies from one model to another. These
 352 two difficulties were tackled by using the RJ-MCMC algorithm (*Denison 2002; Green 1995*). Details
 353 about RJ-MCMC are available in Zhao et al. (*2013*) and not given here.

354 3.4 Posterior inference of changepoints, seasonality, and trends

355 The preceding MCMC algorithm generates a chain of posterior samples of length N
 356 $\{\mathbf{M}^{(i)}, \boldsymbol{\beta}_{\mathbf{M}}^{(i)}, \sigma^{2(i)}, \nu^{(i)}\}_{i=1, \dots, N}$. The chain captures all the information essential for inference of land
 357 dynamics, including trends, seasonal variations, and abrupt changes (Fig. 2). In particular, the
 358 sampled model structure $\mathbf{M}^{(i)}$, such as timings of changepoints and seasonal harmonic orders, can be
 359 directly translated into the model's covariates $\mathbf{x}_{\mathcal{M}^{(i)}}(t)$ (Fig.3), with their associated coefficients
 360 being $\boldsymbol{\beta}_{\mathbf{M}}^{(i)}$. Each sampled model $\mathbf{M}^{(i)}$ gives one estimate of the land dynamics, $\mathbf{x}_{\mathcal{M}^{(i)}}(t) \cdot \boldsymbol{\beta}_{\mathbf{M}}^{(i)}$.
 361 Combining the individual estimates provides not only a final BMA estimate but also uncertainty
 362 measures. The BMA estimate of time-series dynamics is the averaging of all the sampled models:

363 $\hat{y}(t) \approx \frac{\sum_{i=1}^N \mathbf{x}_{\mathbf{M}^{(i)}}(t) \boldsymbol{\beta}_{\mathbf{M}^{(i)}}}{N}$. The associated uncertainty is given as a sample-based variance estimate: $\widehat{\text{var}}[\hat{y}(t)] \approx$
 364 $\frac{\sum_{i=1}^N [\mathbf{x}_{\mathbf{M}^{(i)}}(t) \boldsymbol{\beta}_{\mathbf{M}^{(i)}} - \hat{y}(t)]^2}{N-1}$.

365 Although each single model $\mathbf{M}^{(i)}$ is a piecewise model, the combination of all the individual
 366 models enables the BMA estimate $\hat{y}(t)$ to approximate arbitrary nonlinear signals. Moreover,
 367 because the covariates $\mathbf{x}_{\mathbf{M}^{(i)}}(t)$ and model coefficients $\boldsymbol{\beta}_{\mathbf{M}^{(i)}}$ are simply a coalescing of the individual
 368 elements of the trend and seasonal signals, these elements can be separated to recover the trend and
 369 seasonal components, respectively (Fig. 3).

370 More interestingly, the sampled model structure $\{\mathbf{M}^{(i)}\}_{i=1, \dots, N}$, which is
 371 $\{m^{(i)}, \tau_{k=1, \dots, m^{(i)}}, p^{(i)}, \xi_{k=1, \dots, p^{(i)}}, L_{k=0, \dots, p^{(i)}}\}$, allows making inference and testing hypothesis related to
 372 abrupt changes and land disturbances. Specifically, the chain $\{m^{(i)}\}_{i=1, \dots, N}$ or $\{p^{(i)}\}_{i=1, \dots, N}$ gives an
 373 empirical distribution of the number of changepoints in the trend or seasonal signals; therefore, the
 374 mean total numbers of trend and seasonal changepoints can be estimated as $\bar{m} = \frac{\sum_{i=1}^N m^{(i)}}{N}$ and $\bar{p} = \frac{\sum_{i=1}^N p^{(i)}}{N}$.
 375 For the seasonal signal, the chain of $\{L_{k=0, \dots, p^{(i)}}^{(i)}\}_{i=1, \dots, N}$ can be used to compute the average harmonic
 376 order $\bar{L}(t)$ needed to sufficiently approximate the seasonality for any given time t :

377
$$\bar{L}(t) = \frac{\sum_{i=1}^N L_k^{(i)}}{N}, \text{ subject to } t \in [\xi_k^{(i)}, \xi_{k+1}^{(i)}].$$

378 The use of differing harmonic orders for different times or intervals is a strength distinguishing
 379 BEAST from those algorithms that choose a pre-set, fixed order uniformly for the seasonal signal.

380 In addition, the chains $\{\tau_{k=1, \dots, m^{(i)}}, \xi_{k=1, \dots, p^{(i)}}^{(i)}\}_{i=1, \dots, N}$ indicate the exact timings at which the
 381 trend or seasonal changepoints occurred for the sampled individual models. From these chains, we
 382 can estimate the probability that a changepoint occurs at a time t_s or within a interval $[t_s, t_e]$ by
 383 counting the frequency of the sample $\{\tau_{k=1, \dots, m^{(i)}}^{(i)}\}_{i=1, \dots, N}$ containing the time t_s or falling into $[t_s, t_e]$:

384
$$p(\text{changepoint at } t_s \text{ or within } [t_s, t_e] | \mathcal{D}) \approx \frac{\# \text{ of } \mathcal{M}^{(i)} \text{ that includes } t_s \text{ or falls into } [t_s, t_e]}{N}$$
.

385 Likewise, given an estimated changepoint, we can derive its credible interval. We can also calculate
386 many more sophisticated statistics, such as what is the conditional probability of observing a
387 changepoint in trend at a time if another changepoint has already occurred somewhere, and what is
388 the joint probability of observing a changepoint in trend at one time and a seasonal changepoint at
389 another time? All these sample-based statistics serve as important measures for statistical diagnostics
390 such as uncertainty analysis and hypothesis testing. For example, a changepoint with an estimated
391 occurrence probability of 3% is less likely to represent a true abrupt change.

392 3.5 Software Implementation

393 We implemented BEAST in the C programming language. The core is the MCMC sampler of Eq. 6,
394 an iterative process involving heavy matrix computation such as matrix multiplication and inversion.
395 We tested several matrix libraries and found that Intel's MKL was the fastest. We also implemented
396 an R and a Matlab interface to BEAST: an R package named "Rbeast" is forthcoming. To facilitate
397 algorithm assessment, we further developed a toolkit "trackEcoDyn" (Fig. 10). It offers a graphical
398 user interface (GUI) that allows interactively running BEAST and more importantly, manually
399 analyzing and interpreting Landsat time series data in reference to other image sources (e.g., Landsat
400 images, and aerial photos). The tool is automatically linked with Google Earth and its high-resolution
401 historical imagery, facilitating visually cross-checking land histories among multiple sources. The
402 purpose of trackEcoDyn is to aid in interpreting Landsat time series and collecting ground-reference
403 data for algorithm assessment, as used below in our second case study.

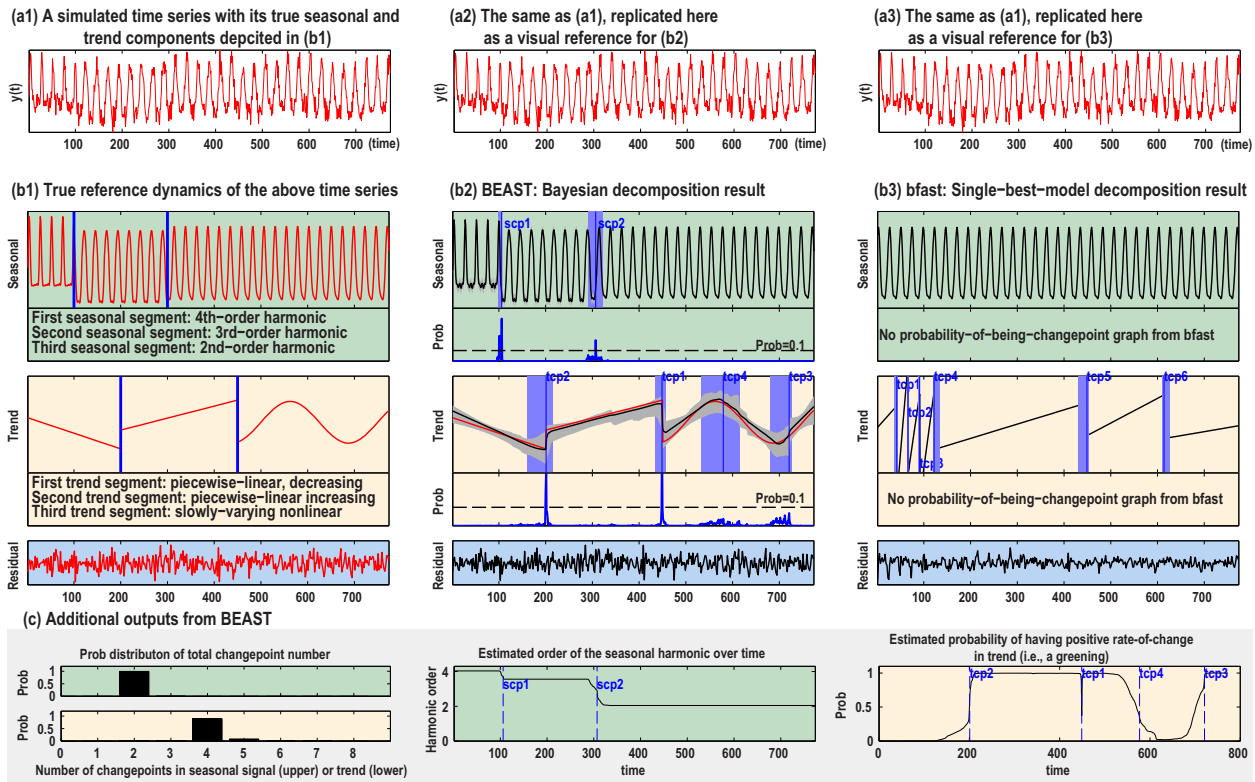
404 4. Examples

405 Three examples are given below to illustrate the basic usage and typical outputs of BEAST. To
406 highlight its differences from existing methods, we also compared BEAST to a community-endorsed
407 algorithm called bfast (*Verbesselt et al. 2010a*). Bfast is a criterion-based method seeking a single best
408 model, as opposed to the Bayesian inference with BEAST. Bfast and BEAST adopt the same general

409 linear model form, thus allowing us to isolate the effects of inference paradigms and remove other
 410 confounding effects on the algorithm comparison. As shall be seen below, despite the use of the same
 411 parametric model, BEAST and bfast disagreed on decomposition results.

412 **4.1 Example 1: A simulated time series**

413 In Example 1, we simulated a time series of length $n=774$ with a period of $P=24$ (Fig. 4a1). In the
 414 simulation, the true reference seasonal signal has two seasonal changepoints (scp), giving three
 415 seasonal segments; the seasonality was simulated using different orders of harmonics for individual
 416 segments (Fig. 4-b1). The true trend has two trend changepoints (tcp), giving three trend segments:
 417 The first two are piecewise-linear; the third is a slow-varying nonlinear continuous signal with no
 418 abrupt jumps (Fig 3a). We chose such a continuous trend for the third segment because this is often
 419 the case for real ecosystem dynamics and the performances of conventional methods for such
 420 nonlinear trends were rarely evaluated in the remote sensing time-series literature.



421

422 Fig. 4. Example 1: Use of a simulated time series (a1-a3) to illustrate BEAST. The true dynamics underlying the time
423 series (b1) were uncovered by BEAST accurately (b2). Specific information estimated by BEAST includes, but is not
424 limited to, seasonal and trend signals, seasonal and trend changepoints (scp or tcp, as denoted by vertical blue bars),
425 and harmonic orders of individual seasonal segments (c, middle). BEAST also provided an array of useful
426 uncertainty diagnostic statistics, such as credible intervals of the estimated signals (i.e., gray envelopes), the
427 probability of observing a scp or tcp at any given time, the probability distribution of total numbers of scp or tcp (c,
428 left), and the probability of having a positive rate-of-change in trend (c, right). For comparisons, the results from the
429 single-best-model algorithm “bfast” are given in (b3). Bfast detected no scp and six tcps.

430 Use of BEAST and bfast is sensitive to the specification of two hyperparameters: maximum
431 number of changepoints (M_{\max})—an upper limit imposed on how many changepoints are allowed in a
432 single model; minimum separation interval (h) —the minimum distance in time allowed between two
433 neighboring changepoints in a single model. In this example, we chose $M_{\max}=8$ and $h=24$ (one
434 period). (In bfast, h is expressed as the ratio of the interval to the time series length.)

435 BEAST uncovered the true dynamics from the simulated time series with high fidelity. The
436 detected signals correlated well with the true references [$r=0.998$ (seasonal) and 0.956 (trend),
437 $n=774$]. BEAST not only successfully pinpointed the two true scps but also correctly identified the
438 differing harmonic orders for the three seasonal segments (Fig. 4c, middle). In the trend, BEAST
439 precisely detected the two reference tcps associated with the piecewise-linear segments. For the third
440 nonlinear trend segment, BEAST additionally detected $2.2 \approx 2$ tcps to capture the sinuous
441 nonlinearity. Because changepoints are defined as any timings at which the trend deviates from its
442 previous linear trajectory (Sect 2), in theory, the nonlinear trend segment of this example is fraught
443 with changepoints through the time. This theoretical expectation aligns well with the BEAST-
444 estimated probability of changepoint occurrence (Fig. 4b2), wherein the estimated probability curve
445 was often nonzero with many small peaks over the third trend segment. All the probabilities were
446 small, indicating the very low likelihood of identifying high-intensity abrupt changes in this nonlinear

447 trend segment, except at the two turning points of the sinuosity. In contrast to BEAST, bfast detected
448 no scps and six tcps (Fig. 4b2).

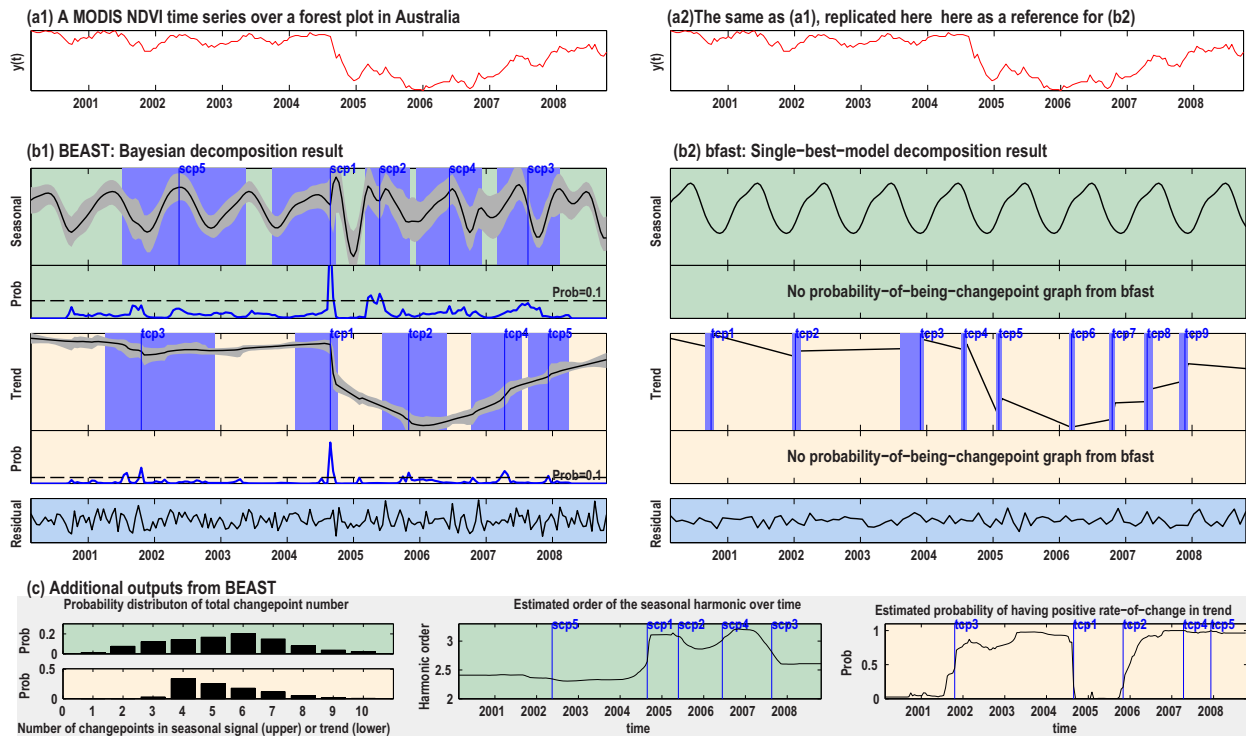
449 BEAST also produced a rich set of uncertainty measures useful to guide the interpretation of
450 inferred dynamics (Figs. 4b2 & 4c). As examples, the synthesis of individual models allows BEAST to
451 generate uncertainties that incorporate both data noises and model misspecification. The inferred
452 trend signal in Fig. 4b2 was not identical to the true signal, but the envelopes of 95% uncertainty
453 intervals enclosed the true signal almost completely, attesting to the utility and reliability of the
454 estimated credible intervals (Fig. 4b2). BEAST tells not only the most likely timings and numbers of
455 tcp or scps but also the probability of observing a scp or tcp for any given time as well as the
456 probability of detecting a certain total number of scps or tcps (Fig. 4c, left). In this example, the
457 probabilities of having 2 scps were 0.9963, leaving only a probability of 0.0037 to find other numbers
458 of scps and suggesting high confidence in pinpointing the two scps.

459 Likewise, BEAST can derive the probability distribution of harmonic orders needed to
460 adequately model a seasonal segment. Another output important for ecological remote sensing is
461 pertinent to the rate of change in trend. For example, BEAST infers not only the sign of the change
462 (e.g., a greening or browning) but also the probability of having a greening or browning at any time
463 (Fig. 4c, right). In essence, for all parameters of interest, BEAST infers not only the most likely
464 values but also the associated error bars and even more, the associated probability distributions, the
465 latter of which are generally impossible to estimate by non-Bayesian algorithms.

466 **4.2 Example 2: A MODIS NDVI time series**

467 Example 2 is based on 9-years' MODIS NDVI data at a forest site in Australia (Fig. 5), which
468 has been used by Verbesselt et al. (2010a) to test bfast. Despite being familiar to large audiences, its
469 true underlying seasonal and trend dynamics are unknown, except that we know that the site
470 experienced droughts in 2001 and 2002 and was harvested in 2004. With all trees removed, the 2004

471 harvest should have altered both the NDVI trend and seasonality. It remains untested whether the
 472 drought effects are detectable from this time series. To run BEAST and bfast, we used a maximum
 473 changepoint number of $M_{\max}=10$ and a minimum inter-changepoint distance of $h=.5$ year.



474
 475 Fig. 5. Example 2: Use of a MODIS NDVI time series in the bfast R package to illustrate the use of BEAST. The true
 476 underlying seasonal and trend signals are unknown, except that we know that this site experienced droughts in 2001
 477 and 2002 and was clear-cut in 2004. BEAST detected 5 scps and 5 tcps, uncovering not only the abrupt changes
 478 from the 2004 clear-cut but also the subtle disturbances associated with the 2001 drought. Phenological changes
 479 resulting from the 2004 clear-cut and the subsequent recovery and forest management activities were captured by a
 480 total of four scps (i.e., scp 1 to 4). For comparisons, bfast found no scp and 9 tcps detected (b2).

481 BEAST unveiled both the large-magnitude and subtle changepoints (Fig. 5b1). On average, it
 482 detected $5.2 \approx 5$ tcps and $5.3 \approx 5$ scps. One of the five tcps is attributed to the drought (i.e., tcp#3) and
 483 the other four attributed to the 2004 harvest and the consequent post-harvest recovery. The five scps
 484 are evidenced in the estimated seasonal trajectory, the seasonal changepoint probability graph, and
 485 the harmonic-order graph. In contrast, bfast detected no scps and 9 tcps.

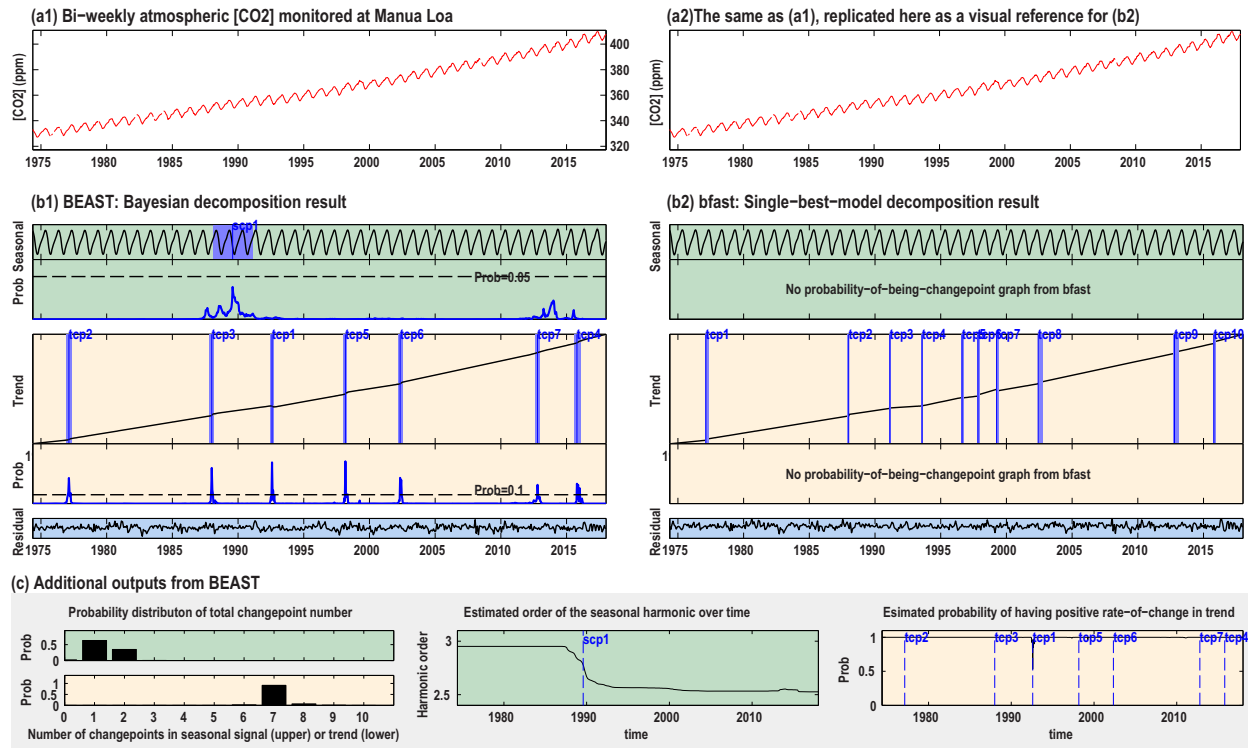
486 BEAST estimated a more parsimonious trend than bfast (i.e., $5.2 < 9$). Despite the
487 parsimony, the BEAST trend captured a complex nonlinear dynamics (Fig. 6b1). As examples, the
488 low-intensity stresses of the 2001 and 2002 droughts were noticeable in the trend. The effect of the
489 2001 drought was found more severe and was associated with tcp#3 in Fig. 5.1. The rapid recovery
490 past the year 2006 was uncovered by BEAST as a continuous nonlinear trajectory, which contrasts
491 with the bfast-detected discontinuous trajectory that has jumps with a browning trend after the year
492 2008. Another salient difference pertains to shifts in seasonality. With the 5 scps detected (Fig. 5b1),
493 BEAST was able to capture the phenological shifts caused by the 2002 drought (scp#5), the 2004
494 logging (scp#1), and the post-harvest recovery (scp#2, 3, &4). In contrast, bfast detected no scp and
495 uncovered a stable seasonal trajectory (Fig. 5b2), suggesting no phenological change before and after
496 the harvest.

497 **4.3 Example 3: CO2 time series at Manua Loa**

498 Example 3 is intended to demonstrate the use of BEAST as a generic algorithm. We considered 45
499 years' bi-weekly atmospheric CO2 measurements from the year 1974 to 2018 at Manua Loa (Fig.
500 7a1). The true trend or seasonal CO2 dynamics are unknown, except that we know there was a rising
501 trend due to human activities and there was a regime shift in the Earth system in the 1980s ([Reid et al.](#)
502 [2016](#)), which should be reflected in the seasonal CO2 dynamics. This knowledge provides valuable
503 information to assess the validity of the decomposition results. For both BEAST and bfast, we chose
504 $M_{\max}=10$ and $h=1$ year.

505 Decomposition results of BEAST and bfast appeared visually similar, but the exact dynamics
506 uncovered by the two differed greatly (Fig. 6). On average, BEAST detected 1 seasonal changepoint
507 (scp) and 7 trend changepoints (tcps); bfast detected no scp and 10 tcps. One of the tcps—detected
508 by both BEAST and bfast—occurred around the year 1977, marking a heightened increase in CO2
509 and coinciding with the start of China's economic reform (Fig. 7b1). This finding is the first time that

510 the carbon footprint of an economic policy has ever been directly pinpointed in a station-based CO2
 511 time series. Exact drivers for other tcps need close scrutiny in future studies.



512
 513 Fig. 6. Example 3: Use of 45 years' atmospheric CO2 data at Manua Loa (a1-a2) to illustrate BEAST for generic
 514 applications. On average, BEAST detected one seasonal changepoint (scp) and 7 trend changepoints (tcps). The true
 515 seasonal or trend CO2 dynamics are unknown, but the BEAST decomposition is consistent with known drivers. The
 516 CO2 trend shifted to a faster rising trajectory around the detected 1977 tcp [i.e., tcp2 in (b1)], coinciding with the
 517 end of China's Cultural Revolution and the start of its economic reform. More interestingly, the detected scp around
 518 the year 1989 (b1, top; c, middle) is consistent with the growing body of evidence that the Earth system saw a
 519 systematic regime shift in the 1980s. For comparisons, the bfast results detected no scp and 10 tcps.

520 The most likely seasonal changepoint (scp) detected by BEAST was found around the year
 521 1989, an abrupt change not detected by bfast (Fig. 6b2). This scp is not too sharp a one but a gradually
 522 transient one spanning multiple years in the 1980s (Fig. 6c, middle). Its presence was indicated in the
 523 scp probability graph (Fig. 6b1). Its occurrence was also evident in the trajectory of estimated
 524 seasonal harmonic orders (Fig. 6c, middle). The detection of this 1989 scp is non-trivial, showing that

525 the global carbon cycle was subject to a regime shift in the 1980s (Figs. 6b1 and 6c). The validity of
526 this shift is supported by a converging body of observational and modeling evidence (*Reid et al. 2016*).
527 A comparison of the BEAST seasonal trajectories before and after 1989 indicates an intensified global
528 carbon cycle over time with a strengthened carbon sink. As a rough estimate, the amplitude in
529 seasonal CO₂ variation increased from 6.35 (pre-1989) to 6.58 ppm (post-1989), a 3.6% increase. The
530 magnitude of peak global carbon sink—estimated as the temporal derivative of the seasonal CO₂
531 trajectories—was enhanced from 26.5 to 27.6 ppm/year. The post-1989 seasonal dynamics also
532 showed some enhanced springtime carbon sink, an advancing in peak sink, and a slight increase in
533 autumn carbon source, all consistent with the recognized effects of global warming on ecosystem
534 productivity (*Piao et al. 2008*).

535 **5. Case Studies and Results**

536 To evaluate BEAST and further exemplify its usefulness for remote sensing applications, we
537 conducted three case studies using either simulated or real data (Figs. 7-11). These case studies were
538 targeted at different aspects of BEAST; each chose a differing type of strategies or reference data for
539 algorithm assessment:

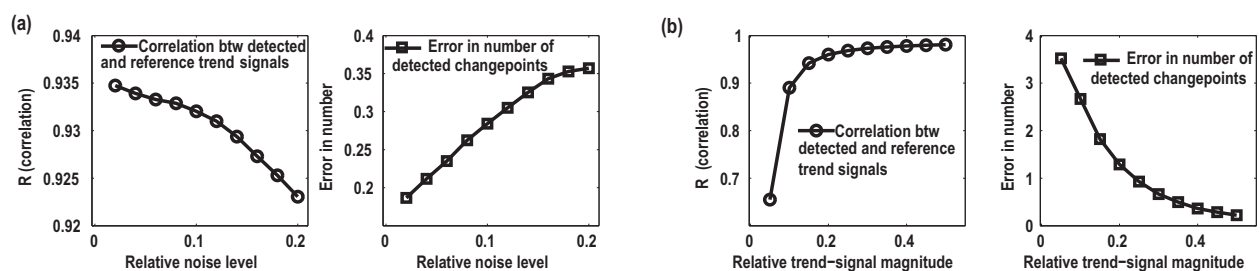
540 (1) Case study 1 used simulated data with true reference dynamics precisely known. The aim is to test
541 how BEAST can uncover the true reference trend signals, an aspect critical for ecological remote
542 sensing but seldom tested before. A secondary aim is to quantify how the performance of BEAST
543 responds to data noises and relative magnitude of trend signals.

544 (2) Case study 2 used dense stacks of Landsat imagery. Ground-reference data on disturbances and
545 changepoints were visually derived from interpretation of multisource imagery following a protocol
546 similar to Cohen et al. (*2011*). The aim is to evaluate the ability of BEAST in detecting disturbances
547 from high-resolution data; trend signals is not evaluated here due to the impossibility of obtaining
548 true reference trend signals.

549 (3) Case study 3 used MODIS EVI data at 250-m resolution over a region where the extents and
 550 timings of two large-scale disturbance events are known. Independent reference data were obtained
 551 from aerial photos or Landsat imagery. The aim is to determine whether BEAST can help to reveal
 552 the disturbance patterns from the MODIS data and also to assess the utility of the probabilistic
 553 information derived by BEAST.

554 5.1 Case study 1: Simulated data

555 Simulated time-series data were generated by additively combining synthetic trend and seasonal
 556 signals, abrupt changes, and random noises. The trends considered were piecewise linear, with
 557 coefficients randomly sampled from a Gaussian distribution; the seasonal signals were piecewise
 558 harmonics, with the order randomly sampled between 1 and 5. The simulation was based on varying
 559 levels of data noises (2% to 20%), relative trend-to-seasonal signal strength (5% to 50%), and
 560 changepoint number (0 to 10). For each combination, we replicated 1000 times with the time-series
 561 length randomly chosen between 200 and 500, with a total of 110,000 time series generated. The use
 562 of such well-controlled data is not only appealing but also necessary for algorithm evaluation because
 563 ground-truthing is rarely available at temporal and spatial scales commensurate with the satellite data.



564
 565 Fig. 7. Case study 1: Assessment of BEAST upon 110,000 simulated reference time series. Two performance metrics
 566 are plotted here—correlation between BEAST-detected and true trend signals and error in the number of detected
 567 changepoints. Positive errors indicate underestimates of the true changepoint numbers. Shown here are the
 568 performances of BEAST at different levels of data noises (a) and relative trend-signal magnitudes (b). Each data
 569 point plot here represents the averaging over 110,000/10=11,000 time series.

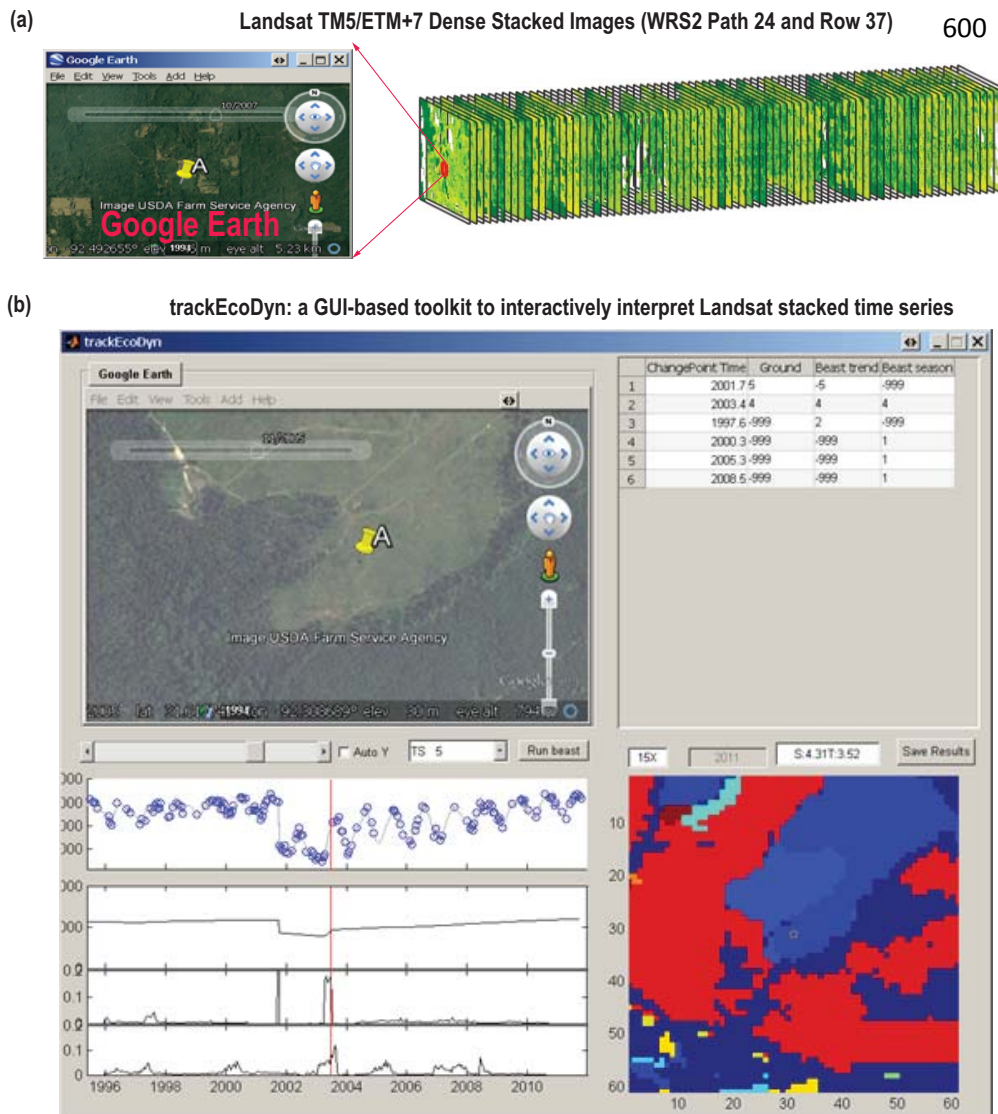
570 BEAST unveiled true trend signals accurately (Fig. 7). When tested upon the simulated data,
571 the estimated trends matched the true signals closely, with a correlation coefficient averaging 0.931.
572 Even for the noisy NDVI simulation with a noise magnitude of 20% (i.e., a signal-to-noise ratio of
573 5.0), BEAST could detect the true trend signals well; the correlation averaged 0.923 (Fig. 7a). In
574 contrast, the estimation of trends showed more sensitivity to relative magnitudes of the trend to
575 seasonal signals (Fig. 7b). For example, when the magnitudes of trends in simulated data were 5% of
576 those of seasonal signals, the correlation between the BEAST-detected and true trends was 0.67
577 ($p < 0.001$); if the relative trend magnitude increased to 10%, the correlation rose to 0.89 ($p < 0.001$).

578 Similarly, BEAST detected changepoints reliably, irrespective of the data noise levels
579 considered (Fig. 7a). However, when the true trend signals became weak and dwarfed by the seasonal
580 signals, detection of trend changepoints became difficult or impossible (Fig. 7b)—a data quality
581 problem that no algorithms can resolve. Therefore, the true changepoint numbers are increasingly
582 underestimated as the trend signal becomes weaker. The problem with weak trends also explains the
583 consistent underestimation pattern for all noise levels (Fig. 7a). The error depicted there at a given
584 noise level is the average over all possible levels of relative trend magnitude; therefore, this error is
585 contributed and dominated by the underestimation associated with those time series with weak trend
586 signals.

587 **5.2 Case Study 2: Dense Landsat Stack**

588 In Case study 2, we acquired 495 images of Landsat TM5 or Landsat 7 ETM+ (WRS2 Path
589 24/Row 37) over the Southern US. We corrected the images radiometrically and atmospherically into
590 surface reflectance via the LEDAPS framework and the FMask cloud masking algorithm (*Schmidt et*
591 *al. 2013; Zhu et al. 2015*); we then computed NDVI and stacked the results. The number of clear-sky
592 dates in the stack averaged 191 across the scene. To assess BEAST, we randomly sampled 200 time
593 series across the scene. This sample was interpreted independently by three analysts to manually

594 identify all potential changepoints to their full capacities using our GUI-based tool “trackEcoDyn”
 595 (Sect 3.5 or Fig. 8). Any inconsistency among the three was reconciled if an agreement could be
 596 reached and otherwise was simply not considered as changepoints. We used the final consensus set as
 597 ground-reference data to assess how well BEAST detects changepoints in Landsat-type images. The
 598 focus here is on evaluating changepoints rather than trend signals, due to the impossibility of
 599 obtaining true reference trend signals.



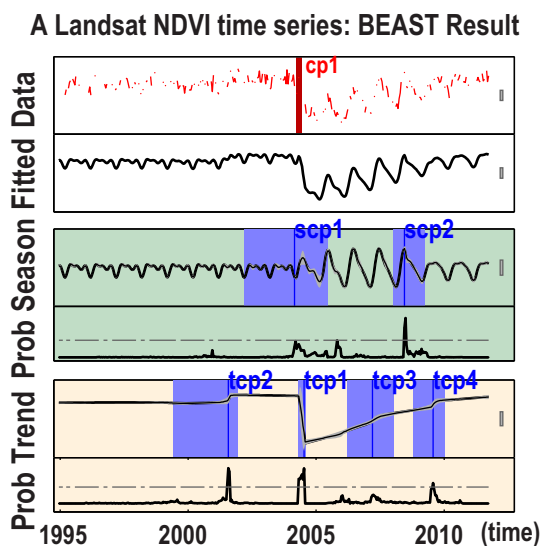
601
 602 Fig. 8. Case study 2: Algorithm assessment based on dense Landsat stack of 495 scenes (WRS2 Path 24/Row 37)
 603 over the Southern US. Shown in (a) is just a subset of the full scene. (b) To collect independent data of land

604 changes, we developed a GUI-based toolkit “trackEcoDyn” through the mixed use of Matlab and C to interactively
605 analyze and interpret Landsat time series. It integrates BEAST and ingests multiple external data sources. Google
606 Earth is also synchronized automatically. This toolkit was built here to help image analysts manually and visually
607 collect reference data for assessing the BEAST algorithm, but it can be equally applied to visually interpret or
608 automatically analyze other spatiotemporal data.

609 BEAST has detected most of the changepoints in the ground-reference data, though with
610 seemingly non-negligible omission and commission errors. In the ground reference for the 200 time
611 series, there were a total of 368 changepoints pinpointed via visual interpretation, including 190
612 disturbance-type events (i.e., declining NDVI) and 178 recovery-type events (i.e., rising NDVI).
613 These reference changepoints were resolved to individual years. As for comparisons, BEAST
614 detected 217 disturbance-type and 197 recovery-type changepoints, all of which were resolved to the
615 sub-monthly level. An automatic matching of the event years showed that the omission and
616 commission errors of BEAST were 17.7% (i.e., a producer accuracy of 82.3%), and 26.8% (i.e., a user
617 accuracy of 73.2%). Examined for disturbance-type events only, the omission and commission errors
618 are 9.5% (i.e., 18/190) and 20.7% (i.e., 45/217); for recovery-type events, the omission and
619 commission errors are 26.6% and 33.5%. It appears that BEAST had larger commission errors than
620 omission errors.

621 The assessment metrics reported above, especially the commission errors, are underestimates
622 of the true capabilities and accuracies of BEAST. As a further evaluation, we manually paired and
623 compared the BEAST results with the ground-reference data. The 18 omission errors out of the 190
624 disturbance-type reference changepoints, as labelled by the automatic matching, were not always true
625 errors. Six of the 18 were not true omissions because BEAST correctly detected them to the sub-
626 monthly level in years different from but immediately adjacent to the years in the ground references;
627 the BEAST-detected timings were more accurate. Likewise, the commission errors reported above

628 are not always true algorithmic errors (Fig. 9). At least three of the 45 disturbance-type changepoints
 629 labeled as commission errors are associated with data anomaly due to cloud contamination: we
 630 expected BEAST to detect these anomalies as changepoints, although they are not ecologically
 631 meaningful. More importantly, many other commission errors are unlikely to be true errors because
 632 BEAST detected all kinds of changepoints of varying intensity but the ground-reference data
 633 included only those visually conspicuous to the analysts. For example, in the recovery trajectory of a
 634 forest plot (Fig. 9), BEAST identified three changepoints that demarcated contrasting succession
 635 stages of the recovery, but the analysts could pinpoint only one changepoint.



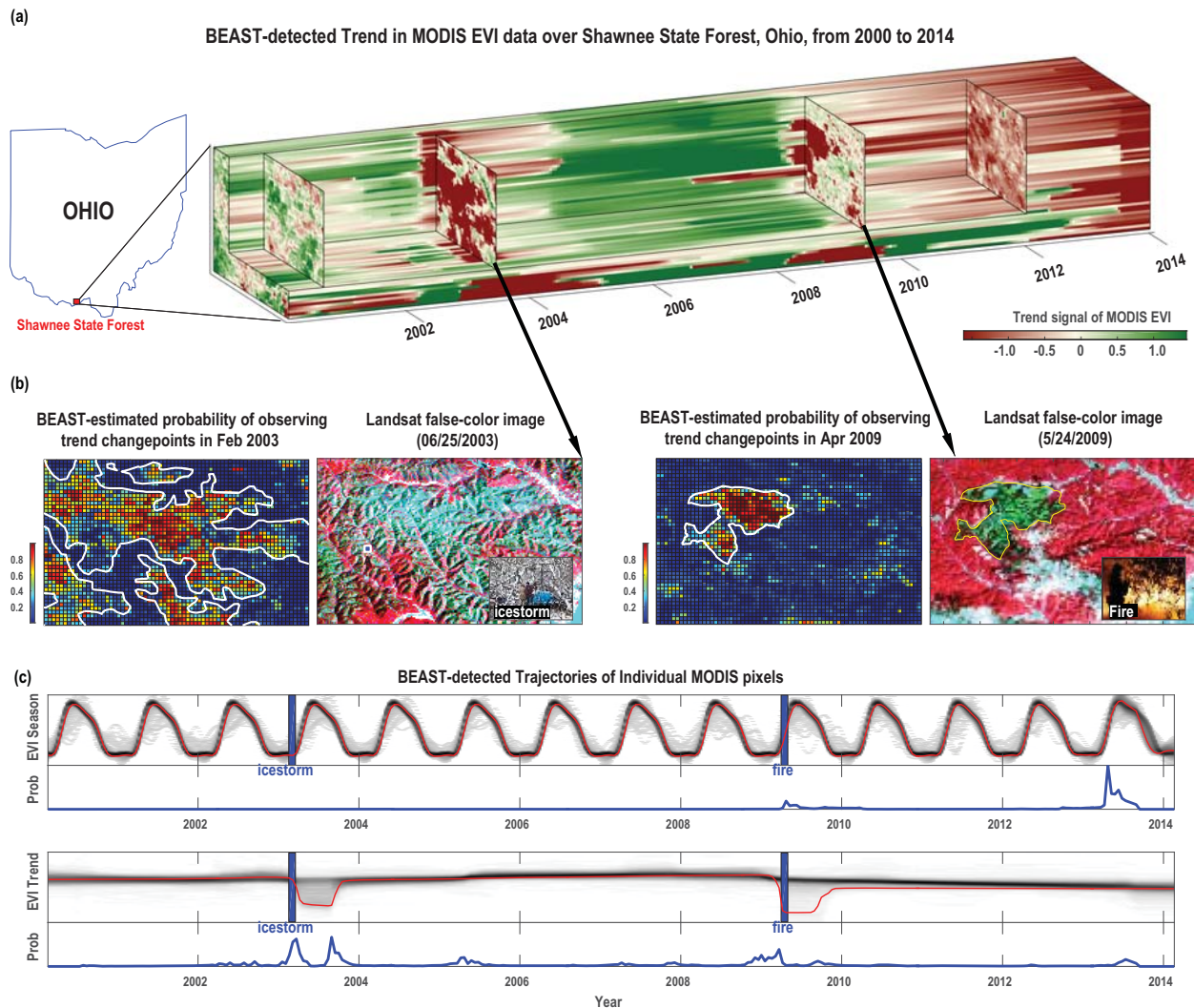
636
 637 Fig. 9. Case study 2: BEAST decomposition of a Landsat time series at a forest pixel as an example to illustrate the
 638 artificial discrepancy in changepoint detection between BEAST and visual interpretation. BEAST found all types of
 639 changepoints—a total of four tcps, being abrupt or gradual. However, when interpreting visually, the three experts
 640 pinpointed only one changepoint (i.e., cp1--the sudden NDVI drop to forest logging). Hence, commission errors of
 641 BEAST in detecting changepoints in reference to the visually-interpreted ground reference are not always true
 642 errors. Illustrated also here is the capability of BEAST for filling data gaps in the Landsat time series.

643 **5.3 Case Study 3: MODIS EVI**

644 The study area chosen here is part of the Shawnee State Forest, Ohio, USA (Fig. 12a). This region
645 has been disturbed or frequently managed across various scales. In particular, the region was struck
646 by an ice storm in Feb 2003 and a fire in April 2009—Ohio’s largest recorded wildfire (Eidenshink et
647 al. 2007). The data we examined were EVI data from MODIS’s 16-day L3 data at 250-m resolution
648 from year 2002 to 2014. To better characterize the disturbance patterns of the ice storm and fire, we
649 also compiled Landsat-5 Thematic Mapper images at 30-m spatial resolution collected before or after
650 the disturbances. The perimeters of the regions disturbed by the ice storm and fire were manually
651 delineated from aerial photos (i.e., white polygons in Fig 10.b). We also calculated the Normalized
652 Burn Ratio from the pre-and post-fire Landsat images and took the difference—dNBR—as an
653 indicator of burn severity. These high spatial-resolution images and information provide independent
654 reference data to evaluate and interpret the MODIS results.

655 When applied to the MODIS data, BEAST uncovered spatiotemporal patterns of vegetation
656 dynamics that were consistent with the known disturbance history (Fig. 10). In particular, the two
657 major landscape-scale disturbances, the 2003 ice storm and 2009 fire, were detected successfully.
658 The estimated disturbance timings matched closely with the true dates (Fig. 10c). The BEAST-
659 detected locations and extents of the disturbances closely resembled those patterns revealed by the
660 post-disturbance Landsat images as well as those manually derived from independent high-resolution
661 imagery. Within the perimeter of the disturbed regions, BEAST depicted the spatial heterogeneity in
662 disturbance magnitude. One such output is the probability of being a true changepoint. For example,
663 when tested for the burned region within the 2009 fire rim, the BEAST-estimated changepoint
664 probability strongly correlated with the independent Landsat-based dNBR ($r=0.66$, $n=288$, p -value
665 $<<0.001$) (Fig. 11a). Such probabilistic outputs enable BEAST to characterize not only those large-
666 magnitude disturbances but also all other disturbances over a continuous range of magnitude. The

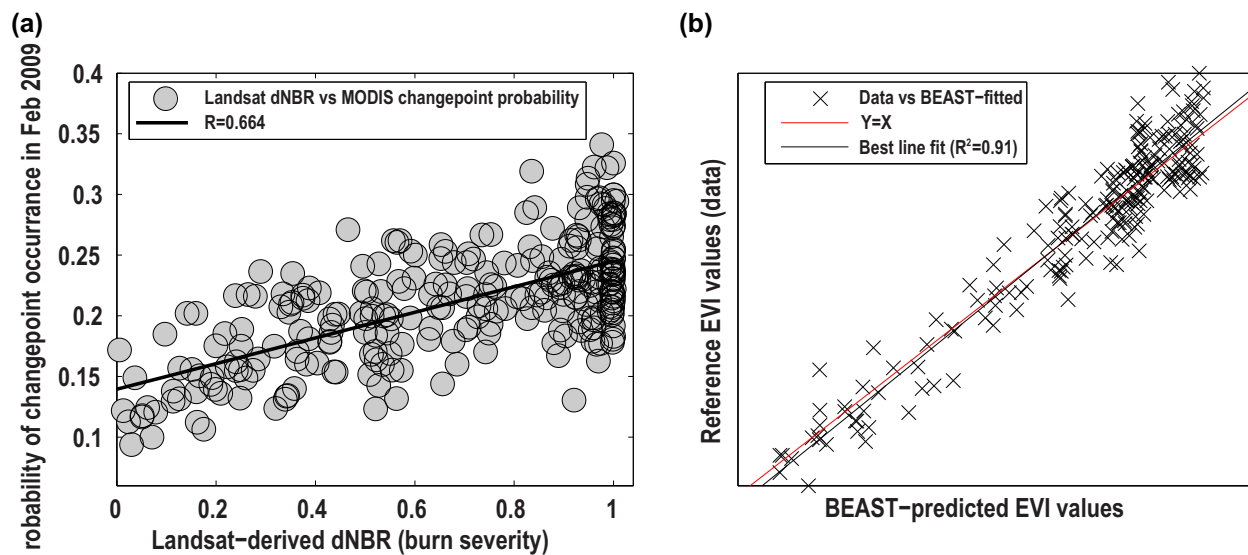
667 probabilistic results should be more informative and practically useful than the mere reporting of
668 binary outcomes about occurrence or not.



669
670 Fig. 10. Case study 3: MODIS EVI data from 2001 to 2014 over the Shawnee State Forest, Ohio where the forests
671 have been disturbed by many natural events and anthropogenic activities, for example, including an ice storm in
672 February 2003 and a fire in April 2009. Shown in (a) is a 3D volumetric view of the spatiotemporal patterns of forest
673 trend dynamics detected by BEAST; therein, brown areas indicate spatiotemporal locations where the forest
674 ecosystem is of low vitality. The ice storm and fire disturbance events are singled out to illustrate the detected
675 probability of changepoint occurrences. (b) Post-disturbance Landsat images together with manually-derived
676 disturbed regions (i.e., white polygons) are accompanied as visual references to assess the spatial patterns of
677 MODIS-based disturbances. Shown in (c) are density plots to depict individual trajectories of detected seasonal and

678 trend dynamics for all the MODIS pixels: the darker the color, the higher the trajectory density. Overlaid on the
 679 density plots are red solid curves to indicate the mean trajectories averaged over all the pixels. The “Prob” subplots
 680 show the mean changepoint-occurrence probabilities averaged over all the pixels (blue curves). The true timings of
 681 the ice storm and fire are indicated by vertical blue bars.

682 Ecologically speaking, the seasonal and trend dynamics uncovered by BEAST were
 683 compatible with true vegetation responses to ice storm and fire. Sudden drops in NDVI were
 684 detected by BEAST at the starts of the ice storm and fire, followed by rapid continuous transient
 685 transitions for post-disturbance recovery. When uncovering seasonal dynamics, BEAST detected no
 686 seasonal changepoints for the 2003 ice storm but some changepoints over part of the region for the
 687 2009 fire (Fig. 10c). This result is corroborated by the contrasting damage severity of the two
 688 disturbances: the ice storm caused branch breakage and infrequent treefall; the fire was more
 689 destructive and sometimes stand-replacing. The severe fire damages shifted the phenology at some
 690 disturbed pixels (Fig. 10c).



691
 692 Fig. 11. Case study 3: (a) BEAST-estimated probabilities of changepoints occurring in Feb 2009 for
 693 288 MODIS pixels within the fringe of the wildfire are correlated significantly with independently

694 derived Landsat burn severity dNBR. (b) True reference EVI values vs. BEAST-estimated values for
695 a selected MODIS time series based on the leave-one-out cross-validation.

696 From a regression standpoint, BEAST fitted the MODIS time series well and made accurate
697 predictions within time-series data gaps. Averaged over all the pixels of the region, the correlation
698 between the actual and fitted time series was 0.943 (Fig. 11a). The strong correlation highlights the
699 predictive power of BEAST and supports its potential use as a gap-filling method. This capability is
700 further confirmed by cross-validation. For example, in Fig. 11b, a leave-out-out cross-validation tested
701 upon a MODIS time series showed that the estimated missing values matched the true reference
702 values with high fidelity ($R^2=0.91$).

703 **6. Discussion**

704 Leveraging the rapid growth of satellite time-series data to uncover the vagaries of landscape change
705 is an area seeing a surge in algorithm development (*Cohen et al. 2017; Wulder et al. 2012; Zhu 2017*).
706 This advance leads to many new ecosystem dynamics products but, at the same time, opens new
707 research gaps (*Cohen et al. 2017*). The problem examined here is how to improve algorithmic
708 robustness and characterize algorithmic uncertainty. Cohen et al. (2017) stressed this problem by
709 noticing considerable discrepancies among seven algorithms, with a pixel-level agreement of only
710 0.2% in detected disturbances and a 1500% difference in estimated disturbance areas. Ensemble
711 learning is touted as a remedy (*Cohen et al. 2018; Healey et al. 2018*) but was only partially explored.
712 The development of BEAST helps to bridge the gap by offering a generic tool that incorporates an
713 ensemble of models into time-series analysis. Our case studies provide experimental evidence on the
714 efficacy of BEAST in detecting abrupt change, seasonality, and trend.

715 **6.1 What BEAST can and can't do?**

716 BEAST is a Bayesian regression method to isolate periodic and trend signals from a time series and to
717 pinpoint abrupt shifts in the two isolated signals. It is intended primarily for trend analysis and

718 changepoint detection, targeted at questions like those elicited in Section 2. Are there any increasing
719 or decreasing trends, any changepoints, or any phenological shifts? What is the rate of change at a
720 given time? Is the detected greening trend real? What is the probability of observing 3 changepoints
721 between 2001 and 2015, or both a seasonal and a trend changepoint in August 2009? Interpretations,
722 connotations, validation of the answers to these questions are context-specific, depending on the
723 goals of applications (Cohen et al. 2017; Wulder et al. 2012). BEAST is applicable to any real-valued
724 variables, such as LAI, temperature, soil moisture, gravity, and other biological or even
725 socioeconomic data; therefore, translating the results into insights is contingent on the natures of the
726 data and problems at hand.

727 BEAST detects temporal dynamics but can't attribute drivers. Is a detected greening due to a
728 warming climate, post-disturbance recovery, or reduced grazing? Is a detected forest loss caused by
729 fire, insect, hurricane, logging, or urbanization? Is a shift in phenology due to climate change, altered
730 management, crop rotation, succession, or land conversion? BEAST can't answer these attribution
731 questions directly. To a lesser extent, even a simple question like whether a detected NDVI drop
732 corresponds to a forest or grass loss can't be answered unless we know that the site observed is a
733 forest or a grassland. To answer the questions, we need to combine BEAST further with other
734 algorithms and ancillary information. For example, BEAST can be used to map extents, timings, and
735 severity of gypsy moth infestation if we know that it is the disturbance agent. For applications on
736 mapping both changes and drivers, BEAST should be interfaced with a classifier that is trained
737 empirically to relate BEAST-derived metrics with land-change classes or causative agents (Cohen et
738 al. 2017). The training and validation of the classifier can follow the good practices recommended for
739 mapping land cover (McRoberts 2011; Olofsson et al. 2014; Olofsson et al. 2013).

740 We envision that BEAST is particularly useful for three related but subtly different areas in
741 remote sensing. One area concerns ecosystem dynamics; the aim is to track vegetation changes over

742 time and understand their drivers. Current use of satellite data for such purposes is fraught with
743 debates, for example, regarding how climate change has affected long-term vegetation growth, how
744 global warming alters land surface phenology, and how extreme weather impacts forests. The second
745 area pertains to mapping land disturbances and land conversion over time. Despite recent advances,
746 the existing algorithms diverged greatly and produced inconsistent disturbance maps. With its proven
747 analytical capability, BEAST should be able to provide new perspectives into these two areas. A third
748 area of applications is to apply BEAST to fill temporal gaps in satellite data. BEAST can fit a
749 nonlinear curve to data with gaps and estimate the missing values.

750 **6.2 BEAST vs. existing methods**

751 Numerous time-series methods have been introduced for applications in remote sensing or other
752 disciplines (*Brockwell and Davis 2016; Hamilton 1994; Zhu 2017*). Many of them were developed
753 under various names, such as trend analysis, seasonal decomposition, changepoint or breakpoint
754 analysis, signal segmentation, regime shift detector, anomaly detection, and structural change
755 (*Brockwell and Davis 2016; Denison 2002; Hamilton 1994; Harvey 1990*). Rigorous comparisons of
756 BEAST to the existing methods are complicated by the sheer number and diversity of algorithms and,
757 to some extent, a lack of consensus on nomenclature. For ease of comparisons, our discussion below
758 focuses only on two aspects of BEAST: trend analysis and changepoint detection.

759 BEAST extends conventional trend analyses in several ways. The majority of existing
760 analyses—based mostly on NDVI—examined linear trends by fitting a global line to the data without
761 considering seasonality, if any (*Brando et al. 2010; Myneni et al. 1997; Piao et al. 2006*). BEAST applies
762 flexible basis functions to fit both linear and nonlinear trends and disentangle trends from seasonality.
763 Some recent trend analysis methods attempted to address nonlinearity using piecewise linear models,
764 but with a prescribed number of changepoints (*Chen et al. 2014; Wang et al. 2011*). A landmark study
765 in this category is Wang et al. (*2011*) that applied a piecewise linear model with one changepoint to

766 AVHRR data for new insights into climate-ecosystem interactions. Indeed, it is the one-changepoint
767 model of Wang et al. (2011) that motivated our algorithm development. BEAST goes beyond by
768 making the changepoint number an unknown parameter and letting the data tell what it is.
769 Statistically speaking, existing analyses were mostly based on frequentist methods, seeking only the
770 “best” model; BEAST employs Bayesian model averaging, embracing all candidate models rather
771 than selecting just one.

772 What distinguishes BEAST most from the existing trend analysis methods is its capability of
773 inferring nonlinear dynamics. BEAST provides a universal approximator of any arbitrarily complex
774 trends. In contrast, most existing methods derive only linear or piecewise linear trends (Wang et al.
775 2011). True drivers of ecosystem dynamics are unlikely to be purely linear or piecewise-linear over
776 time but rather complex and nonlinear. For example, plant successional stages are known to largely
777 follow a nonlinear recovery trajectory (Burkett et al. 2005). Long-term climate trends are confirmed to
778 be inherently nonlinear (Franzke 2014). With its better approximation power, BEAST is more likely
779 to find these true nonlinear trends than the existing methods. Improved fitting of trends can help with
780 changepoint detection because errors in fitting trends may be translated into errors in changepoint
781 detection.

782 For changepoint detection, existing algorithms are mostly heuristically-based, involving the
783 testing or optimization of criteria (Cohen et al. 2017; Zhu 2017). For example, several well-known
784 algorithms, such as LandTrendr, VCT, and CCDC, rely on locally-based heuristic rules by checking
785 if some deviation metrics meet certain pre-set thresholds. They often iteratively analyze the time
786 series piece by piece or step by step (Huang et al. 2010; Kennedy et al. 2010; Zhu et al. 2012). In
787 contrast, BEAST is a parametric regression method. It does not require any threshold testing or
788 criterion optimization but, instead, fits a global model to decompose the whole time series in one step
789 and uncover changepoint , trend, and seasonality altogether. As another key difference, many existing

790 algorithms are hard detectors in that their outputs are limited to either 1 or 0—a changepoint or not;
791 BEAST is a soft/fuzzy detector capable of estimating the occurrence probability of changepoints over
792 time (*Cohen et al. 2017; Huang et al. 2010*). This difference is analogous to that between hard and
793 soft/fuzzy classifiers. To our knowledge, BEAST is the first fuzzy time-series algorithm ever
794 developed for remote sensing applications.

795 Of the existing algorithms, bfast is the one that shares the most commonality with BEAST
796 (*Verbesselt et al. 2010a; Verbesselt et al. 2010b*). The two have almost identical parametric models
797 except that bfast fixes the seasonal harmonic order to a constant of 3 or other constants but BEAST
798 treats it as an unknown to be estimated for individual seasonal segments. This difference seems minor
799 but has substantial effects, partially explaining why BEAST detected more seasonal changepoints.
800 The varying harmonic order gives a flexible representation of seasonality and helps BEAST to
801 capture subtle variations difficult to represent by a fixed-order seasonal model (Fig. 6b1 vs Fig. 6b2).
802 The BEAST or bfast model is additive. If parts of the true seasonal dynamics are not captured by the
803 seasonal model $S(t)$, these seasonal parts will be squeezed into the trend model $T(t)$ or noises. As a
804 result, seasonal abrupt changes may be confused with trend changepoints. Likewise, parts of the true
805 trend, if not adequately captured by $T(t)$, will leak to contaminate the estimation of seasonality. This is
806 why we strived to make BEAST a flexible approximator of any arbitrary trends. In short, reliable
807 detection of changepoints, especially those subtle ones, requires the accurate modeling of not only the
808 trend or seasonal component alone but both altogether.

809 Another key difference between BEAST and bfast or other algorithms lies in parameter
810 estimation. Bfast treats the model parameters as unknown constants. BEAST treats them as random
811 variables; its inferential goal is not only the best values of the parameters—number and timing of
812 changepoints, harmonic orders, and coefficients—but also their probability distributions. BEAST tells
813 not only a detection of 3 tcp but also a 71% probability for having 3 tcps, a 20% for 2 tcps, or a 5% for 1

814 tcp. Put differently, bfast seeks a single best model but BEAST embraces numerous models in terms
815 of a probability distribution over the model space. This is likened to the difference between CART
816 and Random Forests (*Friedman et al. 2001*). Bfast is like CART that finds only one decision tree;
817 BEAST is like Random Forests that uses many trees. As shown in the ecology and machine learning
818 literature, Random Forests is less likely to overfit and more likely to find ecologically-meaningful
819 relationships than does CART (*Breiman 2001a*). Similarly, as an ensemble modeling algorithm,
820 BEAST tends to generate more flexible and interpretable results.

821 **6.3 Ensemble learning: One plus one is more than two**

822 BEAST is based on ensemble learning. Most other algorithms for satellite time-series analysis are not,
823 except two recent algorithms in Cohen et al. (*2018*) and Healey et al. (*2018*). But BEAST and these
824 two are not comparable. BEAST is a regression method for time-series decomposition wherein
825 ensemble learning is internalized into the Bayesian formulation. In contrast, the other two algorithms
826 are some classifiers that ingest the pool of multiple model outputs as predictors to classify disturbance
827 agents. More generally, ensemble learning comes in many other fashions, but the core is to combine
828 many models or algorithms into a better one (*Friedman et al. 2001*). Experimental evidence is
829 unequivocal about the effectiveness and superiority of ensemble learning, compared to the single-
830 best-model paradigm (*Friedman et al. 2001*). Recent years also saw a growing urge for better
831 leveraging the paradigm of ensemble modeling or multi-model inference—a voice that is being heard
832 in many scientific disciplines and is reinforced again here.

833 Why does ensemble learning help with our time-series analysis? The answer lies in a familiar
834 example: the IPCC relies on many climate models instead of any single model to augment confidence
835 in climate prediction (*Solomon 2007*). What is implicit here is George Box’s aphorism “all models are
836 wrong”, a creed that, if held, may help little with practical modeling but, if ignored, can engender
837 unwarranted epistemological debate (*Beven 2010*). All remote sensing models, including radiative

838 transfer models in operational use and our BEAST algorithm, are also wrong in the sense that they
839 are always simplifications and approximations of the true processes (*Schowengerdt 2006*). This is
840 connoted by the fact that remote sensing is fraught with the use of different algorithms or models to
841 decipher the same linkage or functional relationship (*Cohen et al. 2017*).

842 Since all models are wrong, the consideration of many models as in BEAST can reduce the
843 chance of deviating too far from the unknown truth, compared to the choice of just a “best” model.
844 When ranking models in terms of usefulness metrics such as AIC and BIC, the “best” ranked model
845 is not guaranteed to be closer to the truth than other models of lower ranks (*Shmueli 2010; Zhao et al.*
846 *2013*). As a rule of thumb, if two models have an AIC difference of <2.0 , there is no strong evidence
847 that one should be favored over the other (*Burnham and Anderson 2003*). Similar rules exist for other
848 model selection criteria. In the current context, each candidate model is uniquely specified by the
849 model structure parameters, such as numbers and timings of changepoints. The entire model space
850 may comprise quadrillions of candidates or more. Not surprisingly, there can be numerous competing
851 models (e.g., millions) that are statistically indistinguishable from the “best” model in terms of AIC
852 or BIC, a phenomenon called model equalfinality (*Beven 2010*). The lack of strong statistical power to
853 discriminate some models against others makes it safer to use the many models than a “best” model.

854 Even if not all models are wrong and the true model is in the space of candidate models,
855 ensemble learning can still be more robust than single-best-model algorithms (*Friedman et al. 2001;*
856 *Wintle et al. 2003; Zhao et al. 2013*). Even in a simple scenario of linear regression, Zhao et al. (2013)
857 showed that many single-best-model regression procedures failed to recover the true linear model.
858 More generally, no model selection criterion guarantees finding the true model. The failure is
859 primarily due to two factors. First, the space of candidate models is so enormous that optimization
860 may be trapped at local minima, failing to find the real optimal model. Second, even if the real optimal
861 model is luckily found, it may still not be the true model: optimality is not equivalent to truth. The

862 true model may have worse AIC or BIC values than other models, for example, due to data noises or
863 multicollinearity (*Friedman et al. 2001; Grossman et al. 1996*). These difficulties justify the use of
864 ensemble learning even if we can correctly parameterize the true model, let alone when we can't.

865 How can BEAST uncover arbitrary nonlinear vegetation dynamics, given that individual
866 trend models are just piecewise-linear? A rigorous mathematical answer to this is beyond the current
867 scope. Intuitively speaking, the averaging of many piecewise irregular functions will smooth out the
868 irregularity and mold them into a more flexible function (*Friedman et al. 2001*). Indeed, for almost all
869 practical applications, the use of ensemble averaging is more flexible in fitting nonlinear functions
870 than any individual models. A familiar example again is Random Forests: each tree is a discontinuous
871 partition-based function, but the averaging of many trees is able to approximate complex functions
872 (*Cogger 2010*). This is what we call here as “the making of a stronger model from many weak models”
873 or “one plus one is more than two” (*Friedman et al. 2001*). It is this property that enables BEAST to
874 detect realistic vegetation trend dynamics.

875 **6.4 Bayesian statistical modeling: To explain or predict?**

876 BEAST fits a Bayesian regression model or a function curve to match the observed time series, with
877 time as the independent variable. In this regard, BEAST is the same as the many existing statistical
878 models relating remote sensing predictors to biophysical variables. However, their modeling purposes
879 are not the same (*Shmueli 2010*). Most of the statistical models are calibrated to minimize differences
880 between fitted and observed land variables and then estimate the variables for new data unused in the
881 calibration, that is, to predict (*Breiman 2001b; Zhao et al. 2018*). The purpose of BEAST is not to
882 minimize the fitted-vs-observed differences or predict values at a new time but to identify the right
883 mechanisms underlying the observed time series, that is, to explain (*Dashti et al. 2019; Thomas et al.*
884 *2018*). Models that predict well may not explain well, and vice versa (*Shmueli 2010*). Black-box
885 machine learning models are such examples. Although the explain-vs-predict divide is not

886 dichotomous, future studies will garner more successes in designing robust statistical algorithms to
887 obtain useful vegetation dynamics information if we pay attention to the explaining nature of such
888 modeling efforts.

889 Bayesian modeling is of great value in mining complex data to find meaningful and
890 interpretable relationships (*Finley et al. 2008*). A confirmatory example is our BEAST algorithm.
891 Bayesian inference is powerful particularly because of its explicit consideration of various sources of
892 uncertainty (*Denison 2002; Kennedy and O'Hagan 2001*). The time-series problem at hand is a
893 difficult one fraught with uncertainties, due to some apparent conflict. On one hand, model
894 misspecification is inevitable (in theory, true vegetation dynamics are unlikely piecewise-linear or –
895 harmonic); on the other hand, our aim is to use the misspecified model to capture the true vegetation
896 dynamics (the model should explain well). This conflict will be subtly translated into uncertainties in
897 the model parameters and structure. A full characterization of these uncertainties is practically
898 impossible with the conventional single-best-model paradigm, especially because it ignores model
899 uncertainty (*Beven 2010; Kennedy and O'Hagan 2001*). These uncertainties, however, can be
900 formalized and treated rigorously and systematically by the Bayesian paradigm.

901 Despite the exceptional power of Bayesian modeling, its use in remote sensing remains
902 limited. Many factors contribute to this. Philosophically, the “subjective reasoning” label of Bayesian
903 inference may deter many researchers from considering it seriously (*Denison 2002*): who wants to
904 sound subjective in the science enterprise? This concern is unwarranted, given the rising acceptance
905 of Bayesian statistics in essentially all fields after decades of philosophical debate (*Ellison 2004;*
906 *Friedman et al. 2001*). Even if its utility is realized, there is habitual inertia to overcome because
907 conventional statistical methods still find the dominant use. Moreover, the use of Bayesian methods
908 is often hampered more by practical factors, such as a dearth of easy-to-use Bayesian statistical
909 software, the unfamiliarity of these methods to the larger community, the inherent complexity of

910 Bayesian modeling, a lack of formal training in Bayesian statistics, and often enough, daunting
911 computation costs of Bayesian methods. Nonetheless, we hope that the demonstrated value of
912 BEAST provides an impetus to encourage future remote sensing applications of Bayesian techniques.
913 We envision that Bayesian techniques are particularly appealing in cases that data are complex or
914 noisy, characterization of uncertainty is pivotal, computation is not constraining, and the modeling
915 purpose is to explain (e.g., uncover the truth or test theories) rather than predict.

916 **6.5 How to validate time-series decomposition algorithms**

917 What should be validated or evaluated? The goal is to quantify the degrees to which estimated
918 dynamics and changepoints represent the truth. Because changepoints are parts of trend/seasonal
919 signals, validation of changepoints underpins that of trend or seasonal dynamics. In particular,
920 validation of changepoints should cover all the model structure parameters—numbers and timings of
921 changepoints, and harmonic orders. Changepoints here refer to abrupt shifts in both seasonality and
922 trend, be positive or negative in direction, that span a continuous spectrum of magnitude. The
923 changepoints referred to here are consistent with those in Wang et al. (2011) and Browning et al.
924 (2017). This range goes beyond the consideration of only large-magnitude disturbances (e.g., land
925 conversion, forest loss, and fire) that are characteristic of many Landsat-based algorithms (Cohen et
926 al. 2017; Huang et al. 2010). Estimated trend or seasonal dynamics, such as the sign and the rate of
927 change, should be compared to true dynamics.

928 A full evaluation of time-series algorithms such as bfast and BEAST is critical but, often
929 enough, difficult due to a lack of ground-truth (Lu et al. 2004). Take bfast as an example. In the
930 MODIS data of Example 2, only the 2004 trend changepoint (tcp) was originally used to test bfast
931 (Fig. 6) because the 2014 harvest was known precisely. The other tcps and scps were not assessed yet
932 and are hard to test (Fig. 6b2). These tests are about whether the bfast-detected changepoints are real
933 or artificial. A more difficult test is about how many true tcps and scps have been detected by bfast.

934 An even more difficult task is to test the veracity of the estimated trend or seasonal signal. (In Fig.
935 6b2, is the post-harvest browning after tcp#9 a real trend or an algorithmic artifact?) These validation
936 questions are difficult, if not impossible, to answer. The same difficulties apply to validation of
937 BEAST. Similar difficulties were also noted in Browning et al. (2017), which, though considering only
938 15 MODIS time series, is the first study to assess bfast with field-based vegetation dynamics data. But
939 even for that study, the validation was partial, limited to the testing of user accuracy for changepoints.

940 The aforementioned difficulties are manifested in other fashions. Current controversies
941 surrounding satellite-derived ecosystem dynamics could have been safely dismissed if the associated
942 time-series analyses had been validated. Even a seemingly simple question, like “is the NDVI trend a
943 greening or browning?”, has been debated and largely unverifiable. Such issues are not confined to
944 remote sensing. Other fields, such as statistics, ecology, and econometrics, are also fraught with time
945 series analyses of the same nature as ours. We are unaware of any studies in these fields that
946 conducted full validation of changepoint algorithms when tested upon real-world data. For example,
947 many algorithms were applied to the river flow data of the Nile at Aswan (Balke 1993; Betken 2017;
948 Denison 2002; Wu and Zhao 2007). Most of them gave similar but essentially different
949 decompositions. Even for this well-studied data, it is hard to test whether the algorithms uncovered
950 the true river flow dynamics.

951 Because we normally have no access to all the ground-truth needed, we recommend eight
952 practical strategies for algorithm validation. First, a simple yet powerful strategy is to validate
953 algorithms against synthetic data. If an algorithm cannot recover the known true dynamics from the
954 synthetic data to which it is tailored, it unlikely applies well to real data. This test is the first filter that
955 a useful algorithm must pass. Use of synthetic data also permits full assessments under various
956 conditions (e.g., different noise levels) (Section 5.1). Second, algorithms can be validated qualitatively
957 (not equal to “subjectively”) with respect to some general known patterns. This is another filter that

958 useful algorithms must pass. If they detect a declining trend in the air CO₂ data, a browning for forest
959 recovery, or no changepoints for a frequently-disturbed region, there must be some problems with the
960 algorithms. Third, validation can be done using well-established knowledge, such as ecological
961 principles and empirical evidence. One example is the confirmation of the 2004 scp in the MODIS
962 time series because forest clearing is known to change phenology. Another is the 1980s regime shift in
963 the air CO₂ time series. Passing this test will enhance users' confidence in the algorithm. Fourth, as a
964 relative evaluation, an algorithm can be compared to other algorithms. Fifth, cross-validation is
965 another effective strategy, especially for those algorithms that apply parametric models to
966 approximate time series.

967 Sixth, validation can be done using known individual events (e.g., disturbance or land cover
968 change). One example is the evaluation of bfast upon the harvest/planting years over a region in
969 Australia. Our test of BEAST for the fire and ice storm events in Ohio was another example. Seventh,
970 validation can be done using reference data derived from independent sources. One example is
971 through photo-interpretation with TimeSync; another example is our tool trackEcoDyn, which is
972 functionally similar to TimeSync. As a caveat, such reference data are subject to errors and
973 uncertainties (*Cohen et al. 2010*), as explained in Figure 11. Eighth, validation can be done using proxy
974 data of all kinds. One example is the use of climate variables and field-based vegetation composition
975 and biomass in Browning et al. (*2011*) to assess NDVI time series. Another example is our use of
976 dNBR to assess the BEAST-derived changepoint probability. As a third example, to test if surface
977 evaporation sees an abrupt change at a time, we can check air temperature or moisture as proxies.

978 Overall, none of these validation strategies is complete and perfect. A compromise is to rely
979 on as many strategies as possible. Indeed, to test BEAST, we employed all the eight strategies, each
980 emphasizing a differing aspect of BEAST. But in many existing satellite time-series analyses, the
981 practice was to focus only on one aspect of the algorithms (e.g., large-magnitude changepoint only,

982 trend only, or phenology only). Obviously, a comprehensive strategy that embraces more aspects of
983 the algorithms should be preferred because the various components of time-series decomposition do
984 not stand on their own but rather are linked: any errors in one component will be leaked to degrade
985 the estimation of others. Without such comprehensive evaluations, it becomes inevitable that
986 ecological interpretations of satellite time-series decomposition are laden with inconsistency or
987 controversies.

988 **6.6 Caveats and future research**

989 Several caveats are noted. First, BEAST detects anomalies and trends but doesn't attribute the
990 drivers. If data are contaminated by spurious errors (e.g., clouds) or systematic biases (e.g., gradual
991 sensor degradation) (*Wang et al. 2012*), these outliers and drifts can be misconstrued as true signals.
992 To reduce such commission errors, data artifacts should be removed or suppressed beforehand.
993 Second, BEAST makes inference via Monte Carlo sampling and therefore, requiring more
994 computation than many other algorithms (*Kennedy and O'Hagan 2001*). Applications of BEAST to
995 massive high-resolution data, such as the Landsat archive at the global scale, will demand daunting
996 computation. The recommended use of BEAST is for global coarse-resolution or local high-
997 resolution (e.g., Landsat coverage of a county).

998 Third, BEAST explicitly quantifies how likely each point of time is a changepoint. The
999 resultant probability appears indicative of disturbance severity (Fig. 11) and also captures low-
1000 magnitude disturbances that may be missed by other algorithms. Interpretation of the probabilities is
1001 contingent data quality. An abrupt change will have a lower detection probability if data get noisier.
1002 All else being equal, the higher the signal-to-noise ratio, the larger the estimated probability of the
1003 same disturbance. The interpretation is also confounded by sub-pixel heterogeneity. A changepoint
1004 detected with a 5% probability at a pixel, for example, may be due to either a low-magnitude
1005 disturbance across the whole pixel or contrastively, from a severe disturbance over a small fraction of

1006 the pixel. BEAST can't distinguish the two cases. The confounding can be resolved by turning to
1007 finer-grained data (*Roy et al. 2014; Zhao et al. 2018*).

1008 Fourth, the scale matters. When detecting changepoints, BEAST is scale-dependent.
1009 Consider two adjacent pixels, one with a sudden NDVI drop and the other with a rise of the same
1010 magnitude at the same time. If applied separately, BEAST will detect a changepoint for each pixel.
1011 But if the two pixels are combined into one, the two abrupt changes cancel out and the changepoint
1012 disappears at the aggregated scale. This scaling effect is an inherent characteristic of all algorithms.
1013 On the contrary, we speculate that BEAST is scale-invariant when uncovering trends or seasonal
1014 dynamics. That is, applying BEAST to many pixels and then aggregating the individual detected
1015 trends should give the same overall trend as that obtained by first aggregating the individual pixels
1016 into a large pixel and then applying BEAST to the aggregated pixel. This nice property is attributed to
1017 the additive nature of general linear models (*Zhao et al. 2009*). The scale-invariance permits the use of
1018 BEAST across scales to infer trends without introducing artificial discrepancies, thereby facilitating
1019 fusion of multi-resolution data. For applications concerning only trends not changepoints, the use of
1020 BEAST at aggregated scales will also lessen the computation needed.

1021 Fifth, BEAST is applicable to any real-valued data. However, it is a univariate method and
1022 can't decompose multiple time series simultaneously or leverage the inter-correlatedness of the many
1023 time series (e.g., multispectral bands). Extending BEAST into a multivariate algorithm is
1024 conceptually easy but the implementation is complex—a future topic to be explored. Other
1025 extensions are also possible. Here we tested BEAST upon only dense time series to track both trend
1026 and seasonality. It can be revised to handle sparser non-periodic time series (e.g., annual Landsat data
1027 with one observation per year) by simply suppressing the seasonal component in its formulation.
1028 BEAST can also be extended to handle data collected at irregular time intervals or data with duplicate
1029 measurements at a single time. As an unsupervised decomposition algorithm, BEAST can't classify

1030 disturbance agents (*Kennedy et al. 2015*); therefore, another extension is to embed a supervised
1031 classifier into BEAST for simultaneously detecting changepoints and classifying disturbance types.

1032 Last, we highlighted the unique features of BEAST but our intent is not to favor or
1033 discriminate one algorithm against others. All the algorithms have their own niches and offer different
1034 perspectives. Algorithmically speaking, there is no panacea for inferring true dynamics from noisy
1035 data (*Breiman 2001b*). The validity of the diverse or conflicting perspectives, therefore, needs to be
1036 judged based on domain-specific knowledge and high-fidelity ground-truthing. Because BEAST is the
1037 first ensemble-based fuzzy time series decomposition algorithm ever developed for remote sensing
1038 applications and also because it is able to recover complex dynamics and characterize various types of
1039 uncertainty, its use can engender new insights not obtainable by other algorithms. Future studies may
1040 further test the utility of BEAST for various data, problems, and geographic regions. One example is
1041 the analysis of AHVRR or MODIS data to detect disturbances and nonlinear long-term dynamics and
1042 determine how ecosystems have been driven by climate change and human activities, an area still
1043 fraught with many conflicting findings. Overall, BEAST serves a useful tool to derive observational
1044 information from satellite data, as a way to complement field surveys, controlled experiments, and
1045 computer models in quantifying ecosystem responses to environmental changes.

1046 **7. Summary**

1047 We presented a Bayesian algorithm—BEAST—for decomposition of time series into three
1048 contrasting components: abrupt change, periodic change, and trend. BEAST helps to leverage the
1049 increasing availability of multisource satellite time-series data for detecting land disturbances and
1050 tracking nonlinear ecosystem dynamics. Compared to many existing algorithms, BEAST explicitly
1051 addresses model uncertainties via ensemble learning, thereby alleviating inter-algorithm
1052 inconsistencies to some extent. Such inconsistencies were widely recognized and, if not addressed,
1053 would result in diverging or conflicting interpretations of the same data. Conceptually, BEAST

1054 combines many individual weak models into a better model via Bayesian model averaging.
 1055 Mathematically, BEAST is rigorously formulated, with its key equations being analytically tractable.
 1056 Practically, BEAST can estimate probabilities of changepoint occurrence, detect not only large but
 1057 also low-magnitude disturbances, and uncover complex nonlinear trend dynamics, all of which are
 1058 difficult to obtain by single-best-model algorithms. BEAST is generically applicable to not only
 1059 remote sensing data but other environmental, ecological, or socioeconomic time-series data. Our
 1060 initial experiments confirm the utility of BEAST. We envision that its use will offer new satellite-
 1061 based insights into patterns and drivers of ecosystem dynamics.

1062 **Appendix A.**

1063 Here we described more on the specification of the prior $\pi(\boldsymbol{\beta}_M, \sigma^2, M) = \pi(\boldsymbol{\beta}_M, \sigma^2 | M)\pi(M)$ for
 1064 BEAST.

1065 First, we chose a normal-inverse Gamma distribution as the prior of model coefficients $\boldsymbol{\beta}_M$
 1066 and variance σ^2 conditional on model configuration M:

$$\pi(\boldsymbol{\beta}_M, \sigma^2 | M) = \pi_{\beta}(\boldsymbol{\beta}_M | \sigma^2, M) \pi_{\sigma^2}(\sigma^2) = \mathbb{N}(\boldsymbol{\beta}_M; \mathbf{0}_M, \sigma^2 v \mathbf{I}_M) \cdot \mathbb{IG}(\sigma^2; \underline{a}, \underline{b}).$$

1067 where the conditional prior $\pi_{\beta}(\boldsymbol{\beta}_M | \sigma^2, M)$ is a Gaussian distribution $\mathbb{N}(\boldsymbol{\beta}_M; \mathbf{0}_M, \sigma^2 v \mathbf{I}_M)$; the prior
 1068 π_{σ^2} is an inverse-gamma distribution $\mathbb{IG}(\sigma^2; \cdot, \cdot)$ that is independent of the model configuration M and
 1069 is specified by two scalar hyperparameters \underline{a} and \underline{b} . To parameterize the Gaussian prior $\pi_{\beta}(\cdot)$, we set
 1070 its prior mean to zeros $\mathbf{0}_M$, a justifiable choice if the covariates are centered beforehand; the prior
 1071 covariance we chose is the ridge prior $\sigma^2 v \mathbf{I}_M$. The subscript ‘‘M’’ in the zero-mean vector $\mathbf{0}_M$ and
 1072 the identity matrix \mathbf{I}_M indicates that their dimensions depend on the model structure M. Moreover, in
 1073 the prior covariance for $\pi_{\beta}(\cdot)$, v is a scalar hyperparameter. Judicious values for v are not available in
 1074 advance; therefore, we also treated v as random and further assigned it an inverse-gamma prior

1075 $\pi_v(v) = \mathbb{I}\mathbb{G}(v; \underline{c}, \underline{d})$ with two hyperparameters \underline{c} and \underline{d} . This prior $\pi_v(v)$ is a hyperprior because it is
 1076 elicited at a level deeper than β_M . Consequentially, the full conditional prior of Eq. 5 is refurnished as

$$\begin{aligned} \pi(\beta_M, \sigma^2, v | M; \underline{a}, \underline{b}, \underline{c}, \underline{d}) \\ = \pi_{\beta_M}(\beta_M | \sigma^2, v, M) \pi_{\sigma^2}(\sigma^2 | \underline{a}, \underline{b}) \pi_v(v | \underline{c}, \underline{d}) \end{aligned}$$

1077 where the hyperparameters \underline{a} , \underline{b} , \underline{c} , and \underline{d} are underlined and made explicit for the respective priors.

1078 Second, the prior on model structure $\pi(M)$ is chosen to be vague in order to reflect a lack of
 1079 prior knowledge on when and how many abrupt changes occur in an observed time series. Because of
 1080 the separate parameterization for the trend and seasonal signals, it is reasonable to independently
 1081 elicit the model priors for the trend and season signals:

$$1082 \quad \pi(M) = \pi(\{m\} \cup \{\tau_j\}_{j=1, \dots, m}) \pi(\{p\} \cup \{\xi_k\}_{k=1, \dots, p} \cup \{L_k\}_{k=0, \dots, p}).$$

1083 Firstly, the prior for the trend can be decomposed as

$$1084 \quad \pi(\{m\} \cup \{\tau_j\}_{j=1, \dots, m}) = \pi(\{\tau_j\}_{j=1, \dots, m} | m) \pi(m).$$

1085 As a way to encode the vagueness of these model priors, we assume that the number of changepoints,
 1086 m , takes any integer with an equal probability a priori. Meanwhile, we impose a constraint on the
 1087 maximum number of changepoints allowable in a trend signal, as denoted by $\underline{m_{max}}$, which helps to
 1088 preclude over-complicated models. The prior $\pi(m)$ is therefore a uniform distribution over
 1089 $\{0, 1, \dots, \underline{m_{max}}\}$:

$$1090 \quad \pi(m) = \begin{cases} 1/(\underline{m_{max}} + 1) & \text{if } 0 \leq m \leq \underline{m_{max}} \\ 0 & \text{if } m > \underline{m_{max}} \end{cases}$$

1091 Further, given a total of m changepoints, their locations, $\{\tau_j\}_{j=1, \dots, m}$ are assumed to take random
 1092 values from the points of observation time $\{t_i\}_{i=1, \dots, n}$. This choice again represents a non-informative
 1093 prior. As a practical constraint, we assume that any consecutive changepoints should be separated
 1094 apart by at least a time interval \underline{T} . Put together, the conditional prior for changepoint locations is

1095
$$\pi(\{\tau_j\}_{j=1,\dots,m} | m) \propto \begin{cases} 1 & \text{if } \max_{(i,j)} |\tau_i - \tau_j| < \underline{T} \\ 0 & \text{otherwise} \end{cases}.$$

1096 Secondly, the prior on the seasonal model structure can be re-written as

1097
$$\pi(\{p\} \cup \{\xi_k\}_{k=1,\dots,p} \cup \{L_k\}_{k=0,\dots,p}) = \pi(\{\xi_k\}_{k=1,\dots,p} | p) \pi(p) \prod_{k=0}^p \pi(L_k)$$

1098 where the priors on the number and locations of changepoints, $\pi(p)$ and $\pi(\{\xi_k\}_{k=1,\dots,p} | p)$, take the
 1099 same forms as those of the trend signal, except that the maximum number of changepoints allowable is
 1100 \underline{p}_{max} rather than \underline{m}_{max} and that the minimum separable distance between adjacent changepoints is
 1101 \underline{W} rather than \underline{T} . Similarly, the prior on the order of the piecewise harmonic model, $\pi(L_k)$, is also
 1102 considered non-informative in that L_k randomly takes any value between pre-defined lower and upper
 1103 limits of the allowable orders (\underline{L}_{min} and \underline{L}_{max}):

1104
$$\pi(L_k) = \begin{cases} 1/(\underline{L}_{max} - \underline{L}_{min} + 1) & \text{if } \underline{L}_{min} \leq L_k \leq \underline{L}_{max} \\ 0 & \text{otherwise} \end{cases}.$$

1105 In the prior above, the model parameters $\{\beta_{\mathbf{M}}, \sigma^2, v, \mathbf{M}\}$ are of inferential interest and are all
 1106 considered random. In contrast, the ten underlined hyperparameters
 1107 $\{\underline{a}, \underline{b}, \underline{c}, \underline{d}, \underline{m}_{max}, \underline{p}_{max}, \underline{T}, \underline{W}, \underline{L}_{min}, \underline{L}_{max}\}$ are treated as fixed and should be pre-specified, although it
 1108 is permissible to additionally treat them as random variables by further eliciting hyperprior
 1109 distributions at higher levels in a manner similar to the treatment of v . There are no general rules on
 1110 how to specify the values of these hyperparameters. The setup in this study was chosen as $\underline{a} = \underline{b} =$
 1111 $0.01, \underline{c} = \underline{d} = 0.02, \underline{T} = \underline{W} = 1 \text{ year}, \underline{L}_{min} = 0, \underline{L}_{max} = 10, \underline{m}_{max} = \underline{p}_{max} = \max(n/P, 30)$ with
 1112 n and P being the total number of observations and the period of the NDVI signal, respectively. Such
 1113 choices for the inverse gamma priors are almost equivalent to non-informative priors for practical
 1114 purposes, reflecting our vague knowledge on σ^2 or v a priori. Preliminary trials with various datasets
 1115 suggest that the resulting predictive performances are insensitive to the settings of these

1116 hyperparameters as long as \underline{m}_{max} , \underline{p}_{max} , and \underline{L}_{max} assumes a moderately large value (e.g., $\underline{m}_{max} >$
 1117 15, and $\underline{L}_{max} > 6$), $\{\underline{a}, \underline{b}, \underline{c}, \underline{d}\}$ take small values, and the data are standardized beforehand.

1118 As a recap of the Bayesian formulation for BEAST, the likelihood Eq. 4 and the priors Eqs.5
 1119 and 7 combine to reach the full posterior of our formulation according to Eq. 3:

$$1120 \quad p(\beta_M, \sigma^2, v, M | \mathcal{D}) \propto$$

$$1121 \quad \prod_{i=1}^n N(y_i; \mathbf{x}_M(t_i) \beta_M, \sigma^2) \pi_\beta(\beta_M | \sigma^2, v, M) \pi_{\sigma^2}(\sigma^2 | \underline{a}, \underline{b}) \pi_v(v | \underline{c}, \underline{d}) \pi(\{\tau_j\}_{j=1, \dots, m}, m | \underline{m}_{max}, \underline{T}) \pi(\{\xi_k\}_{k=1, \dots, p}, p | \underline{p}_{max}, \underline{W}) \prod_{k=0}^p \pi(L_k | p, L_{min}, L_{max}).$$

1122 It can be further factored into three conditional posteriors:

$$1123 \quad p(M | v, \mathcal{D}) \propto p(\mathcal{D} | v, M) \cdot \pi(M);$$

$$1124 \quad p(\beta_M, \sigma^2 | v, M, \mathcal{D}) = \mathbb{N}(\beta_M; \mathbf{V}_M^* \mathbf{X}_M^T \mathbf{y}, \sigma^2 \mathbf{V}_M^*) \cdot \mathbb{IG}(\sigma^2; \underline{a} + \frac{n}{2}, \underline{b} + [\mathbf{y}^T \mathbf{y} - \mathbf{y}^T \mathbf{X}_M \mathbf{V}_M^* \mathbf{X}_M^T \mathbf{y}]);$$

$$1125 \quad p(v | \beta_M, \sigma^2, M, \mathcal{D}) = \mathbb{IG}\left(v; \underline{c} + \frac{p_M}{2}, \underline{d} + \frac{\sum_{k=1}^{p_M} \beta_{k,M}^2}{2}\right)$$

1126 where we have $\mathbf{V}_M^* = (v^{-1} \mathbf{I}_M + \mathbf{X}_M^T \mathbf{X}_M)^{-1}$ and p_M is the total number of coefficients collected for all
 1127 segments of the piecewise linear and harmonic models. These three conditional posteriors were
 1128 sampled iteratively to simulate a chain of posterior samples using our hybrid Gibbs MCMC sampler.

1129 References

- 1130 Alcaraz-Segura, D., Chuvieco, E., Epstein, H.E., Kasischke, E.S., & Trishchenko, A. (2010). Debating the
 1131 greening vs. browning of the North American boreal forest: differences between satellite datasets.
 1132 *Global Change Biology*, 16, 760-770
- 1133 Balke, N.S. (1993). Detecting level shifts in time series. *Journal of Business & Economic Statistics*, 11, 81-
 1134 92
- 1135 Banner, K.M., & Higgs, M.D. (2017). Considerations for assessing model averaging of regression
 1136 coefficients. *Ecological Applications*, 27, 78-93
- 1137 Betken, A. (2017). Change point estimation based on Wilcoxon tests in the presence of long-range
 1138 dependence. *Electronic Journal of Statistics*, 11, 3633-3672
- 1139 Beven, K. (2010). *Environmental modelling: An uncertain future?* : CRC Press
- 1140 Brando, P.M., Goetz, S.J., Baccini, A., Nepstad, D.C., Beck, P.S., & Christman, M.C. (2010). Seasonal and
 1141 interannual variability of climate and vegetation indices across the Amazon. *Proceedings of the*
 1142 *National Academy of Sciences*, 200908741
- 1143 Breiman, L. (2001a). Random forests. *Machine learning*, 45, 5-32
- 1144 Breiman, L. (2001b). Statistical modeling: The two cultures (with comments and a rejoinder by the
 1145 author). *Statistical science*, 16, 199-231
- 1146 Brockwell, P.J., & Davis, R.A. (2016). *Introduction to time series and forecasting*. springer

1147 Brooks, E.B., Thomas, V.A., Wynne, R.H., & Coulston, J.W. (2012). Fitting the multitemporal curve: A
1148 Fourier series approach to the missing data problem in remote sensing analysis. *IEEE transactions on*
1149 *Geoscience and Remote Sensing*, *50*, 3340-3353

1150 Brooks, E.B., Wynne, R.H., Thomas, V.A., Blinn, C.E., & Coulston, J.W. (2014). On-the-fly massively
1151 multitemporal change detection using statistical quality control charts and Landsat data. *IEEE*
1152 *transactions on Geoscience and Remote Sensing*, *52*, 3316-3332

1153 Browning, D.M., Maynard, J.J., Karl, J.W., & Peters, D.C. (2017). Breaks in MODIS time series portend
1154 vegetation change – verification using long - term data in an arid grassland ecosystem. *Ecological*
1155 *Applications*

1156 Burkett, V.R., Wilcox, D.A., Stottlemeyer, R., Barrow, W., Fagre, D., Baron, J., Price, J., Nielsen, J.L., Allen,
1157 C.D., & Peterson, D.L. (2005). Nonlinear dynamics in ecosystem response to climatic change: case
1158 studies and policy implications. *Ecological complexity*, *2*, 357-394

1159 Burnham, K.P., & Anderson, D.R. (2003). *Model selection and multimodel inference: a practical*
1160 *information-theoretic approach*. Springer Science & Business Media

1161 Cade, B.S. (2015). Model averaging and muddled multimodel inferences. *Ecology*, *96*, 2370-2382

1162 Cai, Z., Jönsson, P., Jin, H., & Eklundh, L. (2017). Performance of Smoothing Methods for Reconstructing
1163 NDVI Time-Series and Estimating Vegetation Phenology from MODIS Data. *Remote Sensing*, *9*, 1271

1164 Chen, B., Xu, G., Coops, N.C., Ciais, P., Innes, J.L., Wang, G., Myneni, R.B., Wang, T., Krzyzanowski, J., & Li,
1165 Q. (2014). Changes in vegetation photosynthetic activity trends across the Asia–Pacific region over
1166 the last three decades. *Remote Sensing of Environment*, *144*, 28-41

1167 Cogger, K.O. (2010). Nonlinear multiple regression methods: a survey and extensions. *Intelligent Systems*
1168 *in Accounting, Finance and Management*, *17*, 19-39

1169 Cohen, W.B., Healey, S.P., Yang, Z., Stehman, S.V., Brewer, C.K., Brooks, E.B., Gorelick, N., Huang, C.,
1170 Hughes, M.J., & Kennedy, R.E. (2017). How Similar Are Forest Disturbance Maps Derived from
1171 Different Landsat Time Series Algorithms? *Forests*, *8*, 98

1172 Cohen, W.B., Yang, Z., Healey, S.P., Kennedy, R.E., & Gorelick, N. (2018). A LandTrendr multispectral
1173 ensemble for forest disturbance detection. *Remote Sensing of Environment*, *205*, 131-140

1174 Dashti, H., Glenn, N.F., Ustin, S., Mitchell, J.J., Qi, Y., Ilangakoon, N.T., Flores, A.N., Silván-Cárdenas, J.L.,
1175 Zhao, K., & Spaete, L.P. (2019). Empirical Methods for Remote Sensing of Nitrogen in Drylands May
1176 Lead to Unreliable Interpretation of Ecosystem Function. *IEEE transactions on Geoscience and*
1177 *Remote Sensing*

1178 Denison, D.G. (2002). *Bayesian methods for nonlinear classification and regression*. John Wiley & Sons

1179 Eidenshink, J., Schwind, B., Brewer, K., Zhu, Z., Quayle, B., & Howard, S. (2007). 1145801. A project for
1180 monitoring trends in burn severity. *Nutrition and cancer*, *58*, 28-34

1181 Ellison, A.M. (2004). Bayesian inference in ecology. *Ecology letters*, *7*, 509-520

1182 Finley, A.O., Banerjee, S., & Carlin, B.P. (2007). spBayes: an R package for univariate and multivariate
1183 hierarchical point-referenced spatial models. *Journal of Statistical Software*, *19*, 1

1184 Finley, A.O., Banerjee, S., Ek, A.R., & McRoberts, R.E. (2008). Bayesian multivariate process modeling for
1185 prediction of forest attributes. *Journal of Agricultural, Biological, and Environmental Statistics*, *13*,
1186 60

1187 Franklin, J., Serra-Diaz, J.M., Syphard, A.D., & Regan, H.M. (2016). Global change and terrestrial plant
1188 community dynamics. *Proceedings of the National Academy of Sciences*, *113*, 3725-3734

1189 Franzke, C.L. (2014). Warming trends: Nonlinear climate change. *Nature Climate Change*, *4*, 423

1190 Friedman, J., Hastie, T., & Tibshirani, R. (2001). *The elements of statistical learning*. Springer series in
1191 statistics New York

1192 Green, P.J. (1995). Reversible jump Markov chain Monte Carlo computation and Bayesian model
1193 determination. *Biometrika*, *82*, 711-732

1194 Grossman, Y., Ustin, S., Jacquemoud, S., Sanderson, E., Schmuck, G., & Verdebout, J. (1996). Critique of
1195 stepwise multiple linear regression for the extraction of leaf biochemistry information from leaf
1196 reflectance data. *Remote Sensing of Environment*, *56*, 182-193

1197 Hamilton, J.D. (1994). *Time series analysis*. Princeton university press Princeton, NJ

1198 Harvey, A.C. (1990). *Forecasting, structural time series models and the Kalman filter*. Cambridge
1199 university press

1200 Hawbaker, T.J., Vanderhoof, M.K., Beal, Y.-J., Takacs, J.D., Schmidt, G.L., Falgout, J.T., Williams, B.,
1201 Fairaux, N.M., Caldwell, M.K., & Picotte, J.J. (2017). Mapping burned areas using dense time-series
1202 of Landsat data. *Remote Sensing of Environment*, *198*, 504-522

1203 Healey, S.P., Cohen, W.B., Yang, Z., Brewer, C.K., Brooks, E.B., Gorelick, N., Hernandez, A.J., Huang, C.,
1204 Hughes, M.J., & Kennedy, R.E. (2018). Mapping forest change using stacked generalization: An
1205 ensemble approach. *Remote Sensing of Environment*, *204*, 717-728

1206 Hu, T., Zhao, T., Shi, J., Wu, S., Liu, D., Qin, H., & Zhao, K. (2017). High-Resolution Mapping of
1207 Freeze/Thaw Status in China via Fusion of MODIS and AMSR2 Data. *Remote Sensing*, *9*, 1339

1208 Huang, C., Goward, S.N., Masek, J.G., Thomas, N., Zhu, Z., & Vogelmann, J.E. (2010). An automated
1209 approach for reconstructing recent forest disturbance history using dense Landsat time series
1210 stacks. *Remote Sensing of Environment*, *114*, 183-198

1211 Huete, A.R., Didan, K., Shimabukuro, Y.E., Ratana, P., Saleska, S.R., Hutyrá, L.R., Yang, W., Nemani, R.R.,
1212 & Myneni, R. (2006). Amazon rainforests green - up with sunlight in dry season. *Geophysical
1213 research letters*, *33*

1214 Jamali, S., Jönsson, P., Eklundh, L., Ardö, J., & Seaquist, J. (2015). Detecting changes in vegetation trends
1215 using time series segmentation. *Remote Sensing of Environment*, *156*, 182-195

1216 Jentsch, A., Kreyling, J., & Beierkuhnlein, C. (2007). A new generation of climate - change experiments:
1217 events, not trends. *Frontiers in Ecology and the Environment*, *5*, 365-374

1218 Jetz, W., Cavender-Bares, J., Pavlick, R., Schimel, D., Davis, F.W., Asner, G.P., Guralnick, R., Kattge, J.,
1219 Latimer, A.M., & Moorcroft, P. (2016). Monitoring plant functional diversity from space. *Nature
1220 plants*, *2*

1221 Jiang, B., Liang, S., Wang, J., & Xiao, Z. (2010). Modeling MODIS LAI time series using three statistical
1222 methods. *Remote Sensing of Environment*, *114*, 1432-1444

1223 Jong, R., Verbesselt, J., Schaepman, M.E., & Bruin, S. (2012). Trend changes in global greening and
1224 browning: contribution of short - term trends to longer - term change. *Global Change Biology*, *18*,
1225 642-655

1226 Jonsson, P., & Eklundh, L. (2002). Seasonality extraction by function fitting to time-series of satellite
1227 sensor data. *IEEE transactions on Geoscience and Remote Sensing*, *40*, 1824-1832

1228 Kennedy, M.C., & O'Hagan, A. (2001). Bayesian calibration of computer models. *Journal of the Royal
1229 Statistical Society: Series B (Statistical Methodology)*, *63*, 425-464

1230 Kennedy, R.E., Andréfouët, S., Cohen, W.B., Gómez, C., Griffiths, P., Hais, M., Healey, S.P., Helmer, E.H.,
1231 Hostert, P., & Lyons, M.B. (2014). Bringing an ecological view of change to Landsat - based remote
1232 sensing. *Frontiers in Ecology and the Environment*, *12*, 339-346

1233 Kennedy, R.E., Yang, Z., Braaten, J., Copass, C., Antonova, N., Jordan, C., & Nelson, P. (2015). Attribution
1234 of disturbance change agent from Landsat time-series in support of habitat monitoring in the Puget
1235 Sound region, USA. *Remote Sensing of Environment*, *166*, 271-285

1236 Kennedy, R.E., Yang, Z., & Cohen, W.B. (2010). Detecting trends in forest disturbance and recovery using
1237 yearly Landsat time series: 1. LandTrendr—Temporal segmentation algorithms. *Remote Sensing of
1238 Environment*, *114*, 2897-2910

1239 Li, L., Vrieling, A., Skidmore, A., Wang, T., & Turak, E. (2018). Monitoring the dynamics of surface water
1240 fraction from MODIS time series in a Mediterranean environment. *International Journal of Applied*
1241 *Earth Observation and Geoinformation*, *66*, 135-145

1242 Liu, D., Toman, E., Fuller, Z., Chen, G., Londo, A., Zhang, X., & Zhao, K. (2018). Integration of historical
1243 map and aerial imagery to characterize long-term land-use change and landscape dynamics: An
1244 object-based analysis via Random Forests. *Ecological Indicators*, *95*, 595-605

1245 Lu, D., Mausel, P., Brondizio, E., & Moran, E. (2004). Change detection techniques. *International Journal*
1246 *of Remote Sensing*, *25*, 2365-2401

1247 Martínez, B., & Gilabert, M.A. (2009). Vegetation dynamics from NDVI time series analysis using the
1248 wavelet transform. *Remote Sensing of Environment*, *113*, 1823-1842

1249 McRoberts, R.E. (2011). Satellite image-based maps: Scientific inference or pretty pictures? *Remote*
1250 *Sensing of Environment*, *115*, 715-724

1251 Myneni, R.B., Keeling, C., Tucker, C.J., Asrar, G., & Nemani, R.R. (1997). Increased plant growth in the
1252 northern high latitudes from 1981 to 1991. *Nature*, *386*, 698

1253 Olofsson, P., Foody, G.M., Herold, M., Stehman, S.V., Woodcock, C.E., & Wulder, M.A. (2014). Good
1254 practices for estimating area and assessing accuracy of land change. *Remote Sensing of*
1255 *Environment*, *148*, 42-57

1256 Olofsson, P., Foody, G.M., Stehman, S.V., & Woodcock, C.E. (2013). Making better use of accuracy data
1257 in land change studies: Estimating accuracy and area and quantifying uncertainty using stratified
1258 estimation. *Remote Sensing of Environment*, *129*, 122-131

1259 Oreskes, N., Shrader-Frechette, K., & Belitz, K. (1994). Verification, validation, and confirmation of
1260 numerical models in the earth sciences. *Science*, *263*, 641-646

1261 Pettorelli, N., Laurance, W.F., O'Brien, T.G., Wegmann, M., Nagendra, H., & Turner, W. (2014). Satellite
1262 remote sensing for applied ecologists: opportunities and challenges. *Journal of Applied Ecology*, *51*,
1263 839-848

1264 Piao, S., Ciais, P., Friedlingstein, P., Peylin, P., Reichstein, M., Luyssaert, S., Margolis, H., Fang, J., Barr, A.,
1265 & Chen, A. (2008). Net carbon dioxide losses of northern ecosystems in response to autumn
1266 warming. *Nature*, *451*, 49

1267 Piao, S., Mohammat, A., Fang, J., Cai, Q., & Feng, J. (2006). NDVI-based increase in growth of temperate
1268 grasslands and its responses to climate changes in China. *Global Environmental Change*, *16*, 340-348

1269 Powell, S.L., Cohen, W.B., Healey, S.P., Kennedy, R.E., Moisen, G.G., Pierce, K.B., & Ohmann, J.L. (2010).
1270 Quantification of live aboveground forest biomass dynamics with Landsat time-series and field
1271 inventory data: A comparison of empirical modeling approaches. *Remote Sensing of Environment*,
1272 *114*, 1053-1068

1273 Raftery, A.E., Gneiting, T., Balabdaoui, F., & Polakowski, M. (2005). Using Bayesian model averaging to
1274 calibrate forecast ensembles. *Monthly Weather Review*, *133*, 1155-1174

1275 Rankin, B.M., Meola, J., & Eismann, M.T. (2017). Spectral Radiance Modeling and Bayesian Model
1276 Averaging for Longwave Infrared Hyperspectral Imagery and Subpixel Target Identification. *IEEE*
1277 *transactions on Geoscience and Remote Sensing*, *55*, 6726-6735

1278 Reiche, J., de Bruin, S., Hoekman, D., Verbesselt, J., & Herold, M. (2015). A Bayesian approach to
1279 combine Landsat and ALOS PALSAR time series for near real-time deforestation detection. *Remote*
1280 *Sensing*, *7*, 4973-4996

1281 Reid, P.C., Hari, R.E., Beaugrand, G., Livingstone, D.M., Marty, C., Straile, D., Barichivich, J., Goberville, E.,
1282 Adrian, R., & Aono, Y. (2016). Global impacts of the 1980s regime shift. *Global Change Biology*, *22*,
1283 682-703

1284 Roy, D.P., Wulder, M., Loveland, T.R., Woodcock, C., Allen, R., Anderson, M., Helder, D., Irons, J.,
1285 Johnson, D., & Kennedy, R. (2014). Landsat-8: Science and product vision for terrestrial global
1286 change research. *Remote Sensing of Environment*, *145*, 154-172

1287 Samanta, A., Ganguly, S., Hashimoto, H., Devadiga, S., Vermote, E., Knyazikhin, Y., Nemani, R.R., &
1288 Myneni, R.B. (2010). Amazon forests did not green - up during the 2005 drought. *Geophysical*
1289 *research letters*, 37

1290 Schmidt, G., Jenkerson, C., Masek, J., Vermote, E., & Gao, F. (2013). Landsat ecosystem disturbance
1291 adaptive processing system (LEDAPS) algorithm description. In: US Geological Survey
1292 Schowengerdt, R.A. (2006). *Remote sensing: models and methods for image processing*. Academic press
1293 Shen, M. (2011). Spring phenology was not consistently related to winter warming on the Tibetan
1294 Plateau. *Proceedings of the National Academy of Sciences*, 108, E91-E92

1295 Shmueli, G. (2010). To explain or to predict? *Statistical science*, 25, 289-310

1296 Shu, L., Jiang, Q., Zhang, X., & Zhao, K. (2017). Potential and limitations of satellite laser altimetry for
1297 monitoring water surface dynamics: ICESat for US lakes. *International Journal of Agricultural and*
1298 *Biological Engineering*, 10, 154-165

1299 Solomon, S. (2007). *Climate change 2007-the physical science basis: Working group I contribution to the*
1300 *fourth assessment report of the IPCC*. Cambridge University Press

1301 Su, Y., Guo, Q., Xue, B., Hu, T., Alvarez, O., Tao, S., & Fang, J. (2016). Spatial distribution of forest
1302 aboveground biomass in China: Estimation through combination of spaceborne lidar, optical
1303 imagery, and forest inventory data. *Remote Sensing of Environment*, 173, 187-199

1304 Tewkesbury, A.P., Comber, A.J., Tate, N.J., Lamb, A., & Fisher, P.F. (2015). A critical synthesis of remotely
1305 sensed optical image change detection techniques. *Remote Sensing of Environment*, 160, 1-14

1306 Thomas, R.Q., Jersild, A.L., Brooks, E.B., Thomas, V.A., & Wynne, R.H. (2018). A mid - century ecological
1307 forecast with partitioned uncertainty predicts increases in loblolly pine forest productivity.
1308 *Ecological Applications*, 28, 1503-1519

1309 Verbesselt, J., Hyndman, R., Newnham, G., & Culvenor, D. (2010a). Detecting trend and seasonal
1310 changes in satellite image time series. *Remote Sensing of Environment*, 114, 106-115

1311 Verbesselt, J., Hyndman, R., Zeileis, A., & Culvenor, D. (2010b). Phenological change detection while
1312 accounting for abrupt and gradual trends in satellite image time series. *Remote Sensing of*
1313 *Environment*, 114, 2970-2980

1314 Wang, D., Morton, D., Masek, J., Wu, A., Nagol, J., Xiong, X., Levy, R., Vermote, E., & Wolfe, R. (2012).
1315 Impact of sensor degradation on the MODIS NDVI time series. *Remote Sensing of Environment*, 119,
1316 55-61

1317 Wang, X., Piao, S., Ciais, P., Li, J., Friedlingstein, P., Koven, C., & Chen, A. (2011). Spring temperature
1318 change and its implication in the change of vegetation growth in North America from 1982 to 2006.
1319 *Proceedings of the National Academy of Sciences*, 108, 1240-1245

1320 Wintle, B.A., McCarthy, M.A., Volinsky, C.T., & Kavanagh, R.P. (2003). The use of Bayesian model
1321 averaging to better represent uncertainty in ecological models. *Conservation Biology*, 17, 1579-1590

1322 Wu, W.B., & Zhao, Z. (2007). Inference of trends in time series. *Journal of the Royal Statistical Society:*
1323 *Series B (Statistical Methodology)*, 69, 391-410

1324 Wulder, M.A., Masek, J.G., Cohen, W.B., Loveland, T.R., & Woodcock, C.E. (2012). Opening the archive:
1325 How free data has enabled the science and monitoring promise of Landsat. *Remote Sensing of*
1326 *Environment*, 122, 2-10

1327 Yu, H., Luedeling, E., & Xu, J. (2010). Winter and spring warming result in delayed spring phenology on
1328 the Tibetan Plateau. *Proceedings of the National Academy of Sciences*, 107, 22151-22156

1329 Zhang, X., & Zhao, K. (2012). Bayesian neural networks for uncertainty analysis of hydrologic modeling: a
1330 comparison of two schemes. *Water resources management*, 26, 2365-2382

1331 Zhao, K., & Jackson, R.B. (2014). Biophysical forcings of land - use changes from potential forestry
1332 activities in North America. *Ecological Monographs*, 84, 329-353

1333 Zhao, K., Popescu, S., & Nelson, R. (2009). Lidar remote sensing of forest biomass: A scale-invariant
1334 estimation approach using airborne lasers. *Remote Sensing of Environment*, 113, 182-196

- 1335 Zhao, K., Popescu, S., & Zhang, X. (2008). Bayesian learning with Gaussian processes for supervised
1336 classification of hyperspectral data. *Photogrammetric Engineering & Remote Sensing*, *74*, 1223-1234
- 1337 Zhao, K., Suarez, J.C., Garcia, M., Hu, T., Wang, C., & Londo, A. (2018). Utility of multitemporal lidar for
1338 forest and carbon monitoring: Tree growth, biomass dynamics, and carbon flux. *Remote Sensing of*
1339 *Environment*, *204*, 883-897
- 1340 Zhao, K., Valle, D., Popescu, S., Zhang, X., & Mallick, B. (2013). Hyperspectral remote sensing of plant
1341 biochemistry using Bayesian model averaging with variable and band selection. *Remote Sensing of*
1342 *Environment*, *132*, 102-119
- 1343 Zhou, T., Popescu, S.C., Lawing, A.M., Eriksson, M., Strimbu, B.M., & Bürkner, P.C. (2017). Bayesian and
1344 Classical Machine Learning Methods: A Comparison for Tree Species Classification with LiDAR
1345 Waveform Signatures. *Remote Sensing*, *10*, 39
- 1346 Zhu, Z. (2017). Change detection using landsat time series: A review of frequencies, preprocessing,
1347 algorithms, and applications. *ISPRS Journal of Photogrammetry and Remote Sensing*, *130*, 370-384
- 1348 Zhu, Z., Wang, S., & Woodcock, C.E. (2015). Improvement and expansion of the Fmask algorithm: Cloud,
1349 cloud shadow, and snow detection for Landsats 4–7, 8, and Sentinel 2 images. *Remote Sensing of*
1350 *Environment*, *159*, 269-277
- 1351 Zhu, Z., & Woodcock, C.E. (2014). Continuous change detection and classification of land cover using all
1352 available Landsat data. *Remote Sensing of Environment*, *144*, 152-171
- 1353 Zhu, Z., Woodcock, C.E., & Olofsson, P. (2012). Continuous monitoring of forest disturbance using all
1354 available Landsat imagery. *Remote Sensing of Environment*, *122*, 75-91

1355

1356